

Flares in Open Clusters with K2.

II. M35, Hyades, and Ruprecht 147

Ekaterina Ilin¹, Sarah J. Schmidt¹, Katja Poppenhäger¹, James R. A. Davenport² and Klaus G. Strassmeier¹

¹ Leibniz Institut für Astrophysik Potsdam

e-mail: eilin@aip.de

² University of Washington e-mail: jrad@uw.edu

Received XXX; accepted XXX

ABSTRACT

Context. Flares can help us trace magnetic activity because are bright and high-contrast on low mass stars.

Aims. This study aims to quantify flaring activity on these stars as a function of mass and age.

Methods. We automatically detected flares in K2 time-domain photometry, using the open-source software K2SC to remove instrumental and astrophysical variability from K2 light curves. We used injection and recovery of synthetic flares to assess detection thresholds, time sampling and de-trending effects on the inferred flare energies. With additional data from the full K2 archive we added stars with a larger variety of ages and spectral types to the analysis of the previous study (Ilin et al. 2019). We compared previous results from the Pleiades and Praesepe to the flare frequency distributions (FFDs) in M35 and the Hyades, respectively. Ruprecht 147 filled in the age gap at 2.5 Gyr between the aforementioned young clusters and the solar age cluster M67.

Results. We find that the flare production mechanism is similar for the entire parameter space, following a power law relation with exponent $\alpha \approx 2$, but the flaring frequencies depend on both mass, and age. We discuss X and Y.

Key words. Methods: data analysis, Stars: activity, Stars: flare, Stars: low-mass

Use \titlerunning to supply a shorter title and/or \authorrunning to supply a shorter list of authors.

1. Introduction

Flares are explosions on stellar surfaces with a complex spatio-temporal and energetic phenomenology. We know that flares are magnetic re-connection events that lead to a change in field line topology and subsequent energy release (Priest & Forbes 2002). We can observe flares in nearly all electromagnetic bands, from radio to X-rays, and on all stars that possess a convection zone. From late F type stars to ultracool dwarfs (Gizis 2013). But even with continuous monitoring at high temporal resolution, the random occurrence of solar flares makes them costly observing targets, especially in coordinated multi-band observations. In integrated light, most solar flares have a far too low contrast and intensity to be observable. Stellar flares on cool stars have two advantages in this respect. They are often bright, enhancing stellar flux by up to several orders of magnitude, and they typically exhibit blackbody emission at temperatures significantly higher than their stars' photospheres. With the evidence that the physical processes that cause flares on the Sun and other stars are the same (Karoff 2016), solar and stellar flares can inform each other (Shibayama et al. 2013). Inconsistencies in extrapolations from solar to stellar conditions (Aarnio et al. 2011; Aarnio et al. 2012; Drake et al. 2012; Alvarado-Gómez et al. 2018). Large surveys like Kepler and TESS enable statistical flare studies of stars that were not pre-selected for their activity (Walkowicz et al. 2011). Statistical studies of stellar flaring activity can help us understand the underlying physical processes CITE stellar surface magnetic fields, starspots (Davenport 2015; Howard

et al. 2019b), how flares relate to stellar angular momentum evolution (Mondrik et al. 2019; Howard et al. 2019b), how they affect the atmospheres of exoplanets (Lecavelier des Etangs et al. 2012; Loyd et al. 2018; Tilley et al. 2019; Howard et al. 2019a), and inform galactic archaeology (Howard et al. 2019a).

Basic parameters that affect flaring behaviour on stars are their masses, and ages. Ages can be controlled for in coeval groups of stars, and flaring-age studies in binaries showed consistency in activity for both components in the majority of targets (Lurie et al. 2015; Clarke et al. 2018). Open clusters present other coeval groups of stars with well-determined ages. Ilin et al. (2019) (hereafter PaperI) investigated the flaring activity of late-K to mid-M dwarfs in three open clusters (OCs), the Pleiades, Praesepe, and M67, using K2 time domain photometry. They analysed the flare frequency distributions (FFDs), with respect to different masses and cluster ages. For the cluster members, the light curves revealed that their flaring activity declines both with age and mass. The decline is faster for higher mass stars. Recently, Davenport et al. (2019) put forward an empirical parametrization of this flaring-mass-age relation based on FFDs. The present study aims to extend the results in PaperI to the age of Ruprecht 147 (2.5 Gyr), and both higher and lower masses than in the previous study. We also test the previous results from the Pleiades on M35, and the results from Praesepe on the Hyades, as both OC pairs have approximately the same ages. Because the Kepler satellite retired in fall 2018, we can now use the complete K2 data set, and supplement all three OCs in PaperI with additional light curves. Additionally, we use high quality K2 light curves available for M67 (Nardiello et al. 2016) and M35 (Soares-Furtado et al. 2017). We discuss our results with

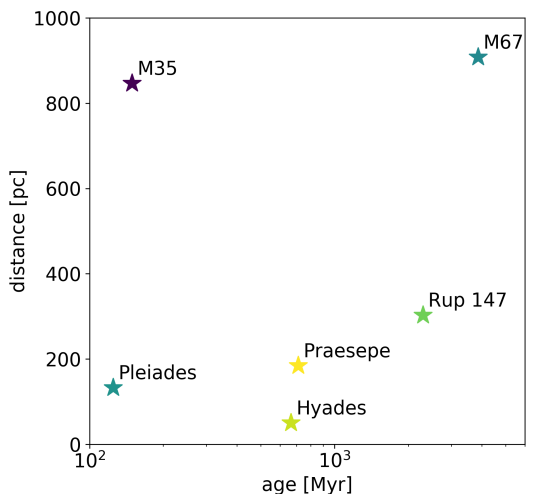


Fig. 1. The values for age, metallicity, and distance are approximate values from a compilation of existing literature, see Appendix B.1.

respect to potential breaks in the power law distribution at high energies. Finally, we use the results to test the parametrizability in Davenport et al. (2019).

2. Data

Our main data are K2 target pixel files that were provided by the Kepler archives hosted at MAST, and light curves derived from them (Aigrain et al. 2016; Soares-Furtado et al. 2017; Vinícius et al. 2018). To assign T_{eff} to the targeted stars we used multi-band photometry obtained from Tycho, UCAC4, 2MASS, Pan-STARRS, and Gaia catalogs. To assign ages to the targeted stars OC membership information was compiled from the literature. An overview over the cluster sample is presented in Table ?? and illustrated in Figure 1.

2.1. K2 light curves

The Kepler (Koch et al. 2010) spacecraft finished its follow-up mission K2 (Howell et al. 2014) in September 2018, after having completed nearly 20 80-day observing campaigns. Even though Kepler and K2 data are used in more than 2 400 publications to date, the public archive can still be considered understudied (Barentsen et al. 2018). In this spirit we took up the analysis of about 4 000 Kepler target pixel files that each contain up to 80 days of 30 min cadence observations in white light ($4, 200 - 9, 000 \text{ \AA}$). We also used light curves extracted from the K2 C0 super stamp. A super stamp is an aggregated set of typical Kepler postage stamps placed over a densely populated field, that also covers M35 (Soares-Furtado et al. 2017).

As K2 was conducted on the two-wheeled Kepler satellite, it was subjected to substantial drift motion (spacecraft roll, Van Cleve et al. 2016) and had an overall reduced pointing accuracy. To mitigate these effects, various solutions were developed (Vanderburg & Johnson 2014; Aigrain et al. 2016; ?; Luger et al. 2018)

2.2. Membership matching

We obtained membership information from multiple catalogs for each cluster. We cross-matched these catalogs on RA and

declination within 3 arcsec. The resulting target lists were used to search the K2 archive, or were matched to the catalogs of extracted light curves from crowded fields in the case of M35 (Soares-Furtado et al. 2017) and M67 (Nardiello et al. 2016).

One part of the membership catalogs provided membership probabilities (Douglas et al. 2014; Bouy et al. 2015; Cantat-Gaudin et al. 2018; Olivares et al. 2018; Reino et al. 2018; Gao 2018; Olivares et al. 2019). For the other part no probability was provided (Rebull et al. 2016a; Douglas et al. 2017; Gaia Collaboration et al. 2018a), or qualitative classifiers were given (Curtis et al. 2013; Gonzalez 2016; Rebull et al. 2017). In the latter cases we assigned approximate probabilities anchored to the set threshold for inclusion into our final sample. Absence in a catalog did not decrease the likelihood of membership, as each catalog shows different selection biases which we did not address in this study. We set the threshold mean membership probability p for a target in our sample to 0.8.

2.3. Open Clusters

We studied flaring activity in the low mass stars in six open clusters spanning from ZAMS to solar age. Table 1 provides an overview over the final sample. The literature overview of age, distance, and metallicity determinations is given in Table ?? in the Appendix. Membership probability histograms of the final sample are displayed in Figure ??.

2.3.1. Pleiades

The Pleiades, a nearby ZAMS cluster, were observed in Campaign 4, and were treated in PaperI. We include the cluster in this work for completeness and to illustrate improvements to (PaperI). We revisited the memberships from Rebull et al. (2016a), which were your in the previous work, and merged them with lists of members determined by Olivares et al. (2018); Gaia Collaboration et al. (2018a); and Cantat-Gaudin et al. (2018).

2.3.2. M35

M35 is a ZAMS cluster 900 pc away, observed during Campaign 0 in K2. We merged membership lists from Cantat-Gaudin et al. (2018); Gaia Collaboration et al. (2018a); and Bouy et al. (2015). There are only five K2 light curves, but we identified multiple additional members with publicly available¹ light curves obtained from Soares-Furtado et al. (2017). They used an image subtraction technique in the campaign's super stamps, a self flat-fielding de-trending inspired by K2SFF (Vanderburg & Johnson 2014), and a trend-filtering algorithm developed by Kovács et al. (2005). We preferred PSF photometry in cases where both aperture K2 and PSF LCs were available. We took the raw extracted PSF light curves and de-trended them using K2SC.

2.3.3. Hyades

The Hyades are a 0.6 Gyr old OC observed during Campaigns 4 and 13 with K2. It is about as old as Praesepe. We merged membership tables obtained from Douglas et al. (2014); Reino et al. (2018); and Gaia Collaboration et al. (2018a).

¹ <https://k2.hatsurveys.org/archive/>

Table 1. Open clusters.

cluster	<i>n</i>	LCs	SLCs	LLCs	PSF LCs	age[Myr]	distance[pc]	[Fe/H]
Pleiades	2033	944	33	911	0	125		
M35	1614	5	0	5	158			
Hyades	655	301	42	259	0			
Praesepe	1281	2500	68	2432	0			
Rup 147	213	97	25	72	0			
M67	1344	1141	118	1023	1019			

Notes. *n* is the approximate number of members with $p > 0.8$. LCs, SLCs, LLCs, and PSF LCs denote the number of available light curves, short cadence light curves, long cadence light curves, and PSF de-detrended light curves, respectively. The values for age, [Fe/H], and distance are approximate values from a comparison of existing literature, detailed in Appendix B.1.

- 149 **2.3.4. Praesepe** 191 E(BP-RP) derived from Gaia photometry and parallax from
150 Praesepe appeared in Campaign 5, and was previously treated 192 Gaia DR2 (Andrae et al. 2018).
151 in PaperI. It was then observed again during Campaign 13. We 193 Using a catalog of touchstone stars, compiled and comple-
152 revisited the memberships obtained by Douglas et al. (2014), and 194 mented by Yee et al. (2017) and the $T_{\text{eff}}-R_*$ relations in Mann
153 matched them to the members identified in Douglas et al. (2017)
195 et al. (2015, 2016). We assigned stellar radii R_* by interpolating
154 Rebull et al. (2017); Cantat-Gaudin et al. (2018); and Gaia Co- 196 between stars that appear in the catalog with similar T_{eff} and
155 laboration et al. (2018a). 197 [Fe/H]. We assigned spectra to our targets from Yee et al. (2017)
198 and the FlareSpecPhot library (Schmidt 2014; Kirkpatrick et al.
199 2010; Burgasser et al. 2007, 2008, 2010, 2004; Cruz et al. 2004;
200 Burgasser & McElwain 2006; Rayner et al. 2009; Doi et al.
201 2010; Filippazzo et al. 2015; Cruz et al. 2003; West et al. 2011;
202 Bochanski et al. 2010, 2007; Schmidt et al. 2010, 2015, 2014;
203 Mann et al. 2015). We then combined stellar radii R_* , T_{eff} , and
204 spectra to projected bolometric luminosities $L_{\text{bol},*}$, and projected
205 luminosities in the Kepler band $L_{Kp,*}$ (Shibayama et al. 2013;
206 Ilin et al. 2019).
207 We applied several methods and color-temperature relations
208 (CTRs) to determine robust T_{eff} . We used CTRs from Boyajian
209 et al. (2013) and Mann et al. (2016) (erratum to Mann et al.
210 2015), and T_{eff} from the StarHorse catalog and Gaia DR2 Apsis.
211 Boyajian et al. (2013) determined CTRs from a range of
212 interferometrically characterized stars using $g - z$, $g - i$, $g - r$,
213 $g - J$, $g - H$, and $g - K$ colors from SDSS and Johnson
214 magnitudes for A to K stars. Their sample is centered on solar
215 metallicity, so we constrained the use of these CTRs to stars with
216 $-0.25 < [\text{Fe}/\text{H}] < 0.25$. We transformed 2MASS JHK to $J - H$,
217 $H - K$, and $J - K$ in the Johnson system as the authors from
218 2MASS to the Bessell-Brett system (Carpenter 2001), and from
219 Bessell-Brett to Johnson using the relations in Bessell & Brett
220 (1988).
221 Mann et al. (2015) provide CTRs from absolutely calibrated
222 spectra to which they fitted atmospheric models to obtain T_{eff} .
223 Alternatively, they determined T_{eff} from long-baseline optical
224 interferometry measurements using the bolometric flux. Among
225 others, they note transformations for SDSS/2MASS $r - z$ and
226 $r - J$, or Gaia $BP - RP$ where extra information can be added
227 from metallicity or 2MASS $J - H$. The relations in Mann et al.
228 (2015) are only valid if metallicity is sufficiently close to solar,
229 which is satisfied for all clusters in this paper (see Table ??).
230 M35 may be an exception to this rule.
231 StarHorse
232 Gaia DR2 published effective temperatures for over 160 million
233 sources (Gaia Collaboration et al. 2018b). The typical uncer-
234 tainty is quoted at 324 K, but it is lower for stars above ~ 4000
235 K and below ~ 6700 K, so that we adopt 175 K which is above
236 the quoted root-median-squared error in this T_{eff} range (Andrae
237 et al. 2018).
238 Empirical CTRs suffer from systematic errors that stem both
239 from the different methods applied, and from sample selection
240 accounted for extinction in Gaia BP and RP using the reddening

240 biases. We used as many empirical relations as possible in their
 241 appropriate ranges to obtain multiple T_{eff} estimates from which
 242 we then drew a more reliable median value. Targets that were
 243 lacking sufficient photometric data to derive T_{eff} , or were too
 244 hot to be expected to have a convective envelope, were flagged
 245 accordingly, and removed from the sample. These excluded data
 246 can be retrieved from the online material.

247 We used a catalog of empirically characterised stars (Yee
 248 et al. 2017) to derive R_* . Yee et al. (2017) collected 404
 249 stars with high-resolution spectra from the literature, and own
 250 observations of mid to late K-dwarfs, spanning low mass stars
 251 from 7000 K down to 3000 K. For these stars, the resulting
 252 catalog is accurate to 100 K in T_{eff} , 15 % in R_* , and 0.09 dex in
 253 [Fe/H]. We matched stars from the catalog to our derived T_{eff}
 254 within uncertainties and propagated the resulting scatter to the
 255 uncertainty in R if $\text{Teff} > 3500$ K. For stars with $\text{Teff} < 3500$ K
 256 we used Mann et al. T-R relations.

257

258 3. Methods

259 We detected and validated flare candidates automatically. We
 260 assigned recovery probabilities and corrected for sampling effects
 261 using injection/recovery tests for different flare morphologies.
 262 Most of the candidates are expected to have a complex shape that
 263 deviates from the classical flare template. The validation yielded
 264 an estimate on the uncertainty on the flare energy released in the
 265 Kepler band. The frequency distributions of these flare energies
 266 are believed to follow a power law that spans multiple orders
 267 of magnitude. We adopted this model, and used two different Max-
 268 imum Likelihood estimators to obtain the power law exponents.
 269 We tested the best fit parameters with the Kolmogorov-Smirnov
 270 test, and probed possible truncation of the power law relation
 271 with an exceedance test.

272 3.1. Flare finding

We used the open source software AltaiPony² to automatically
 297 detect and characterize flares in our sample. The code base
 lies on K2SC³ (Aigrain et al. 2016) to remove instrumental and
 298 astrophysical variability from K2 light curves. We did not use the
 pre-detrended light curves available on MAST, but used K2SC to
 299 derive our own, because we clipped outliers at 3σ , as compared
 300 to the original work, where outliers were clipped at 5σ (Aigrain
 301 et al. 2016).

302 After de-trending, the flare finder algorithm looked for continuous
 303 observing periods, defined as being longer than 10 data
 304 points at a minimum cadence of 2 h. All further routines were
 305 run on these observing periods. The finder iteratively clipped
 306 excursions from the median value at 3σ rolling window noise
 307 above median plus uncertainty given from K2SC de-trending. Af-
 308 ter each iteration, outliers were cut down to the current median
 309 value. Either after convergence, or 50 iterations, the resulting
 310 median value was adopted. With this median, flare candidates
 311 were identified with the same procedure as during the median
 312 value calculation, but now we additionally required at least three
 consecutive data points to fulfil the σ -criterion. Flare candidates
 313 were merged into single candidate events if they were no more
 314 than three data points apart. For each of these candidates, the
 315 amplitude and equivalent duration (ED) was returned.

The Kepler flare sample has shown to be difficult to treat in a

fully automated way. Without manual vetting, the event samples
 remain significantly contaminated (Yang & Liu 2019). We re-
 duce the number of potential false positives using SkyBoT
 ED is the area between the LC and the quiescent flux, that is,
 the integrated flare flux divided by the median quiescent flux F_0
 of the star, integrated over the flare duration (Hunt-Walker et al.
 2012):

$$ED = \int dt \frac{F_{\text{flare}}(t)}{F_0}. \quad (1)$$

ED is a quantity independent of calibration and distance that is
 suited to compare flaring activity on stars where these properties
 are uncertain. It describes the time during which a star releases as
 much energy as the flare itself. This time can be short or longer
 than the actual flare duration.

278 3.2. Recovery probability and ED correction

To further validate the flare events, every candidates was re-
 injected to its light curve of origin several times with varying am-
 plitude and duration using a classical flare template (Davenport
 et al. 2014). This returned a recovery probability of similar flare
 morphologies on a given light curve. We accepted a candidate
 if the recovery probability was above 80 %. From the difference
 between injected and recovered values we calculated individual
 correction factors for all candidates that typically increased the
 ED because the 30 min time sampling systematically underesti-
 mates the ED (Yang et al. 2018) as compared to short cadence
 observations. Corrected flare EDs from injection-recovery vali-
 dated candidates were then converted to $E_{\text{Kp,flare}}$ and passed on to
 further analysis.

How is recovery affected by GP Regression?

Can we isolate sampling effects?

Can we do a simpler correction by showing that most of the
 ED under-estimate comes from the under-sampling at 30 min
 cadence?

3.3. Complex Flares

Complex flares are flaring events that do not follow the classical
 time evolution (Davenport et al. 2014). In many cases, observed
 flares can be described by superimposing multiple single events.
 We call these flares complex. Some flares cannot be described in
 this way. We call these flares atypical. Davenport et al. (2014)
 found 60 – 80 % of flares with duration of more than 50 min to have
 multiple peaks, and successfully fitted them a superposition of
 multiple classical events to them on active M dwarf GJ 1243.
 However, 1.3 % of all flare detections were atypical. In the long
 cadence data present here, flare durations were at least 1.5 h, and
 thus likely most of our candidates have a complex morphology.
 The time resolution, however, bars us from reconstructing the
 individual morphologies directly... *How complex was complex
 (2 flares overlap, or rather 10? Does this depend on energy?*

3.4. Kepler flare energies

(see PaperI for details).

Multiband time resolved observations of active M dwarfs have
 shown that continuum flux accounts for the majority of the
 energy radiated by flares (Kowalski et al. 2013). The effective
 temperature of this blackbody, however, varies by a great degree,
 with, to date, no robust predictor of that temperature:

While solar flares are relatively cool, with

² <https://github.com/ekaterinailin/AltaiPony>

³ <https://github.com/OxES/k2sc>

$T_{\text{eff}} \approx 5000 - 7000$ K (Kleint et al. 2016; Kerr & Fletcher 2014; Watanabe et al. 2013; Namekata et al. 2017), at least one M dwarf flare reached 40 000 K as seen in FUV spectra (Franting et al. 2019), and most events exhibit temperatures of about 9 000 – 10 000 K (Hawley & Fisher 1992; Kretzschmar 2016; Shibayama et al. 2013). A dependence of flare temperature on stellar age, or mass, or both, will enter our analysis if we attempt to quantify bolometric flare energy. At about 6 200 K, the Kepler pass band captures the largest flux fraction, at 10 000 K about 72% at 40 000 K only 4% of this value is transmitted. Another effect is that flares of equal flare energy but hotter SED would not be seen in the Kepler band at all.

We propagated the uncertainties σ_{ED} and σ_L (on $L_{*,Kp}$) quadrature to $E_{Kp,\text{flare}}$. We derived σ_{ED} empirically from the injection and recovery of synthetic flares. It is determined from the standard deviation in correction factors f_{ir} between injected and recovered E_{ir} . f_{ir} is a function of flare amplitude and duration. Uncertainties on amplitude and duration are also derived empirically from injection and recovery of synthetic flares.

We propagated the uncertainties on σ_L from uncertainties in photometry, extinction correction, and empirical color– T_{eff} relations (Mann et al. 2016) for which the photometry was used. Uncertainties on the stellar radius were obtained from T_{eff} – R_{\star} relations (Mann et al. 2016). Both, color– T_{eff} and T_{eff} – R_{\star} relations, included the uncertainties on [Fe/H] that we collected from the literature.

3.5. Power law fits

Flare frequency distributions follow power law relations that cover several orders of magnitude, from solar microflares to stellar superflares. We fitted power law functions to the FFDs using three different approaches. The first method was a maximum likelihood estimator (MLE) from Maschberger & Kroupa (2009). The second method used the MLE result as a prior for α . Following Wheatland (2004), we defined the joint posterior distribution for the probability ϵ that a flare with ED or energy above some value S_2 occurs within a time period ΔT :

$$p(\epsilon, \alpha) = C \cdot (-\ln(1 - \epsilon)^M) \cdot (\alpha - 1)^M \cdot \Gamma(\alpha) \left[\frac{(S_2/S_1)^{M+1}}{\pi} \right]^{\alpha} \cdot (1 - \epsilon)^{(T/\Delta T) \cdot (S_2/S_1)^{\alpha-1} - 1}.$$

C is the normalisation constant, M is the number of events, π is the total observation time. Γ contains the prior distribution for α , and S_1 denotes the detection threshold above which all flares are detected. π encapsulates the flare energies as

$$\pi = \prod_{i=1}^M \frac{s_i}{S_1}$$

, where $\{s_1, s_2, \dots, s_m\}$ are the flare energies or ED . The posterior distribution in Wheatland (2004) captures both Poissonian distribution of flare events in time, and their power law distribution in energy, simultaneously. Wheatland (2004) derived this model to be able to predict the flaring rate of a given active region on the sun, and offered an extension to Eq. 2 that treated changing flaring activity rates as the active region evolves, and also characteristics of the active region itself, such as sunspot classifiers. In our simplification of the model, we assumed that the flare generating process did not change within

the observation time span in any star in our sample ($M = M'$ in Eq. 24 in Wheatland (2004)). Another assumption was that this process was the same for all stars in the sample ($\Lambda_{MC} = 1$ in Eq. 24). Thus the information gained from the light curves could be stacked together.

While in the case of a uniform prior for α the results from the MLE and Markov Chain Monte Carlo (MCMC) sampling from the posterior distribution are the same, the latter allowed us to fit for ϵ and α simultaneously. Additionally, the MCMC approach can be extended to incorporate further information about the stars in the sample in the future.

Another advantage of the latter approach is that we could use more informative priors. We also used a Gaussian fit to α obtained from the posterior distribution using the full sample of flares as the prior for a subsequent Bayesian analysis of individual age and T_{eff} bins. Assuming that α is universal for all spectral types, ages, and flare energy ranges, we used this more informative, Gaussian prior to further constrain the flaring rates.

The uncertainties on α were computed using the jackknife algorithm, which is well suited if we suspect false positives among the flare candidates. The resulting uncertainty estimate reflects the weight of outliers in the data. To show this, we sampled 100 random FFDs of the same size, best fit power law parameters, and minimum and maximum observed ED for each power law fit we performed. We compared the power law parameters derived for these FFDs with the above methods to the original value, and found that the jackknife uncertainty captures XX% of random FFDs' results. With all methods, we fitted the intercept β_{cum} using non-linear least squares to the cumulative FFD and converted the result to $\beta = \beta_{\text{cum}} \cdot |\alpha - 1|$. As with α , we calculated the uncertainty $\sigma_{\beta_{\text{cum}}}$ using the jackknife algorithm, and propagated uncertainties from α for the final result on β .

Additionally we calculated the exceedance statistic tr to test if the power law distribution was truncated. If tr is 1, the power law distribution is truncated at the high energy end. If tr is 0, no information was gained from the calculation. To derive tr , given a number n of observations X_n and a best fit value for the power law exponent, we generated 500 samples with n values from this best-fit distribution assuming no truncation, i.e. choosing an upper limit several orders of magnitude higher than X_{max} . We then proceeded to truncate the samples at thresholds T below the maximum observed value X_{max} and determined the average number N_{ex} of generated values that will exceed T . If the underlying power law is not truncated, N_{ex} declines with larger n , as larger X_{max} will be present in the original data. If the best fit power law exponent is steeper, N_{ex} will be underestimated. If the best fit power law exponent is flatter, N_{ex} will be overestimated. If the power law is not truncated, for $n \geq 100$ N_{ex}/n will be $< 5\%$, for $20 < n < 100$, typically $N_{ex}/n < 15\%$.

As recommended by Maschberger & Kroupa (2009), we applied the stabilized Kolmogorov-Smirnov (KS) test at 95 % significance level to all power law fits in the sample. If the test fails the power law model does not fit the data at the given significance level. If the test passes, this does not give any information whether the power law model is the correct assumption. The goodness of fit can be estimated from the visual inspection of percentile-percentile plots, given in the online material⁴.

4. Results

Fig. 5 shows the $E_{\text{Kp,flare}}$ and ED detection thresholds, as defined by the recovery probability (see Sec. 3.2). The thresholds in ED reflect the noise level in the light curves.

4.1. Flaring activity as a function of age and T_{eff}

Flaring activity decays with age. Flaring fraction was observed to decline with galactic latitude for M dwarfs (Hilton et al. 2010) Howard+2019. Short rotation periods and high magnetic activity measured in $H\alpha$ are strongly correlated (West et al. 2015). According to gyrochronology, fast rotation indicates young age (Barnes 2003), and slows down as the star ages. Here we quantify how this decline unfolds for different spectral types. Except for the stars in our coolest temperature bin (M5.5–M8.2 2 500–3 000 K), stellar flaring activity at a given age is always stronger for a cooler star. The exception is seen at cluster ages around 120 Myr.

4.2. M67

We found one very likely flare candidate in the PSF-detrended light curves (Nardiello et al. 2016). After having searched the entire sample we identified about 250 candidates. We excluded those candidates that clustered spatio-temporally in different light curves as systematics. After vetting the remaining 25 by eye, we excluded false positives judging by their morphology, leaving a mere ten light curves with flare-like shape. One target appeared to be an echo from one of the other light curves. Five targets were foreground stars, two are more likely background stars, one target is probably a giant and does not appear in Gaia photometry (IR source). Only one target appears to reside at M67 distance and is a $p = 0.997$ member according to Gao (2018). The 2MASS and Gaia BP and RP colors indicate an M2V dwarf (Pecaut & Mamajek 2013). If the spectral classification is correct, the flare releases about $6.1 \cdot 10^{33}$ erg ($ED = 1391 \pm 544$ s) in the Kepler band.

4.3. Flaring Activity Indicators

Flaring rates: FR and flaring fraction We define **FR** as the flares rate above detection thresholds on $E_{\text{Kp,flare}}$ and ED in each T_{eff} bin, respectively (Figs. 6 and 7).

Flaring energy: FA and $L_{\text{Kp,flare}}$ The energy released in flares was inferred using our derived stellar luminosities. It declines with age for every T_{eff} bin considered for both the total luminosity and relative to the quiescent flux (Fig. 8).

$L_{\text{Kp,flare}}$ is the luminosity in flares in the Kepler band. We can relate this to the quiescent bolometric luminosity of the star when we define the fractional flare luminosity **FA** as in PaperI:

$$FA = \frac{1}{N} \sum_i^N FA_i = \frac{1}{N} \sum_i^N \frac{E_{\text{Kp,flare,tot},i}}{t_i \cdot L_{\text{bol},*,i}} \quad (4)$$

We determine $L_{\text{bol},*}$ from R_* and T_{eff} , as described in Sec. 2.4. This is a meaningful measure of relative stellar activity as long as only the flux portion of the quiescent star in the Kepler band is roughly constant. It is therefore sensible to compare **FA** values across ages, but not across T_{eff} .

FFD Power law fit parameters to the FFDs (Figs. 9 and 10) are sensitive to the low-energy cutoff, where most observations reside. The goodness of fit strongly depends on the sample size. Power law fit parameters derived using MLEs, as described in Sec. 3.5, are mostly consistent with each other but often deviate from $\alpha = 2$. A smaller sample size tends to create a flatter distribution (Figs. 11 and 12). Truncation was not detected for FFDs with more than 50 flares (Tables 2 and 3). For these results, extrapolations outside of the observed energy range are clearly off. If we assume $\alpha \equiv 2$, different distributions can be compared. For fixed α , in the ED domain, β_2 is the flare frequency at $ED = 1$ s, and shows a trend in both T_{eff} , and age (see Fig. 14). In the energy domain, the picture is less clear (Fig. 13).

Compare to other FFD values, e.g., from Ward’s Evryscope survey, see table in Appendix, and maybe convert it to a plot Howard et al (2019) monitored superflares on cool stars with bolometric energies above 10^{33} erg and up to 10^{36} erg. They find power law exponent values around ~ 2 resolved by spectral types. Similar values are found for individual flare stars (Lurie et al. 2015).

Howard+18, Loyd+18, Tilley+19 show that flares can erode exoplanetary atmospheres. If a flare is assumed to deposit its UV energy in an instant a single superflare can completely remove the ozone layer at the substellar point Loyd+18. Associated protons are safer way to ozone destruction if they are associated with reoccurring large flares Tilley+19

5. Discussion

5.1. Flaring and rotation

More energetic flares can be expected from faster rotating stars (Candelaresi et al. 2014; Doorslaere et al. 2017; Yang et al. 2017). Findings that flares with intermediate Rossby number appear to flare more than fast and slow rotators (Mondrik et al. 2019) could not be reproduced here or in the EvryFlare survey (Howard et al. 2019b). If enhanced flaring can be interpreted as an increase in the stellar angular momentum loss rate flaring activity can be used to inform the cause of variation in the spin-down efficiency. An example of such variations is the apparent temporary stalling of spin-down seen in K dwarfs in NGC 6811 (Curtis+2019). The authors favored a scenario in which the stellar core transfers momentum onto the envelope but did not rule out the possibility of a decreased magnetic braking efficiency. In the latter scenario, these stars should flare less.

We used rotation periods derived from K2 light curves for the Pleiades (Rebull et al. 2016b), the Hyades (Douglas et al. 2016), and Praesepe (Rebull et al. 2017), to illuminate the rotation-flaring relation at fixed ages. In the Pleiades, most flaring stars are found on the fast rotator branch at or below one day, and flaring activity peaks in this regime. For Praesepe, flaring rates appear to [...] In the Hyades, all of the 11 stars with rotation periods that overlapped with our sample were found flaring, but the numbers were too low to provide statistical insight. For Rup 147, M35 and M67, no rotation rates were available at the time.

5.2. M37

Comparing our results to a similar study of photometric flares in M37 (Chang et al. 2015) we find the results somewhat discrepant. M37 is 300–600 Myr old and appears less active than Praesepe and Hyades in individual Teff bins, which are of coeval or older. We attribute the difference to the loose membership requirement of $pmem \geq 0.2$ in Chang et al. (2015) as compared to our stricter cuts at 0.8. We expect the M37 to be contaminated

⁴ <https://github.com/ekaterinailin/flare-in-clusters-with-k2-ii>

Table 2. Summary of activity parameters of all clusters and T_{eff} bins in energy distributions.

cluster	$T_{\text{min}} [\text{K}]$	$T_{\text{max}} [\text{K}]$	n_s	n_{flares}	age [Myr]	[Fe/H]	$E_{\text{Kp,flare,min}} [\text{erg}]$	α_{B}	β_2 [yr^{-1}]	β_{MK} [yr^{-1}]	tr_{B}	tr_{MK}
Pleiades	4000	4999	87	148	125 ± 25	-0.02 ± 0.03	$1 \cdot 10^{34}$	1.70 ± 0.24	1.58 ± 0.20	$7.19 \cdot 10^{33} \pm 2.32 \cdot 10^{32}$	$2.07 \cdot 10^{23} \pm 5.12 \cdot 10^{32}$	$1.39 \cdot 10^{19} \pm 2.87 \cdot 10^{18}$
Pleiades	3000	3249	353	420	125 ± 25	-0.02 ± 0.03	$4.6 \cdot 10^{33}$	1.35 ± 0.42	$6.57 \cdot 10^{32} \pm 1.60 \cdot 10^{31}$	-	$1.09 \cdot 10^{10} \pm 4.74 \cdot 10^9$	0
Pleiades	3250	3499	168	324	125 ± 25	-0.02 ± 0.03	$4.8 \cdot 10^{32}$	2.08 ± 0.12	2.06 ± 0.11	$1.71 \cdot 10^{33} \pm 6.95 \cdot 10^{30}$	$1.97 \cdot 10^{35} \pm 9.34 \cdot 10^{34}$	0
Pleiades	3750	3999	92	125	± 25	-0.02 ± 0.03	$5.2 \cdot 10^{32}$	1.86 ± 0.12	1.83 ± 0.11	$4.01 \cdot 10^{33} \pm 4.99 \cdot 10^{31}$	$8.29 \cdot 10^{27} \pm 9.52 \cdot 10^{26}$	0
Pleiades	5000	5999	53	23	125 ± 25	-0.02 ± 0.03	$3.7 \cdot 10^{32}$	-	$1.51 \cdot 10^{33} \pm 1.56 \cdot 10^{32}$	-	$1.66 \cdot 10^{8} \pm 5.19 \cdot 10^7$	0
Pleiades	3500	3749	50	127	125 ± 25	-0.02 ± 0.03	$3.8 \cdot 10^{32}$	1.74 ± 0.09	1.72 ± 0.09	$4.44 \cdot 10^{33} \pm 8.32 \cdot 10^{31}$	$7.47 \cdot 10^{24} \pm 6.80 \cdot 10^{23}$	$1.93 \cdot 10^{24} \pm 1.70 \cdot 10^{23}$
M35	4000	4999	216	23	149 ± 13	-0.21 ± 0.06	$1.6 \cdot 10^{33}$	1.23 ± 0.32	1.24 ± 0.27	$3.15 \cdot 10^{33} \pm 5.31 \cdot 10^{32}$	$2.20 \cdot 10^6 \pm 7.14 \cdot 10^5$	$4.81 \cdot 10^6 \pm 1.34 \cdot 10^6$
Hyades	4000	4999	32	24	665 ± 70	0.13 ± 0.01	$1.2 \cdot 10^{32}$	-	1.06 ± 0.14	$8.40 \cdot 10^{32} \pm 1.54 \cdot 10^{32}$	-	$1.07 \cdot 10^9 \pm 1.83 \cdot 10^{-1}$
Hyades	3000	3249	54	115	665 ± 70	0.13 ± 0.01	$2.5 \cdot 10^{32}$	1.89 ± 0.18	1.85 ± 0.17	$1.15 \cdot 10^{33} \pm 6.45 \cdot 10^{30}$	$1.93 \cdot 10^{29} \pm 3.51 \cdot 10^{28}$	$1.33 \cdot 10^{28} \pm 2.28 \cdot 10^{27}$
Hyades	3250	3499	42	140	665 ± 70	0.13 ± 0.01	$2.2 \cdot 10^{33}$	2.09 ± 0.65	1.90 ± 0.47	$2.19 \cdot 10^{33} \pm 9.70 \cdot 10^{31}$	$2.06 \cdot 10^{36} \pm 1.33 \cdot 10^{36}$	$1.13 \cdot 10^{30} \pm 5.36 \cdot 10^{29}$
Hyades	3750	3999	5	25	665 ± 70	0.13 ± 0.01	$6.3 \cdot 10^{31}$	1.47 ± 0.23	1.45 ± 0.19	$2.12 \cdot 10^{33} \pm 9.71 \cdot 10^{31}$	$5.41 \cdot 10^{15} \pm 1.24 \cdot 10^{15}$	$1.02 \cdot 10^{15} \pm 2.01 \cdot 10^{14}$
Hyades	5000	5999	11	11	665 ± 70	0.13 ± 0.01	$1.9 \cdot 10^{33}$	-	1.06 ± 0.28	$7.75 \cdot 10^{34} \pm 7.76 \cdot 10^{33}$	-	$1.36 \cdot 10^0 \pm 4.59 \cdot 10^{-1}$
Hyades	3500	3749	14	31	665 ± 70	0.13 ± 0.01	$8.8 \cdot 10^{31}$	1.13 ± 0.24	1.16 ± 0.20	$1.54 \cdot 10^{33} \pm 2.27 \cdot 10^{32}$	$2.29 \cdot 10^3 \pm 5.82 \cdot 10^2$	$2.38 \cdot 10^4 \pm 5.14 \cdot 10^3$

Table 3. Summary of activity parameters of all clusters and T_{eff} bins in equivalent duration distributions.

cluster	$T_{\text{min}} [\text{K}]$	$T_{\text{max}} [\text{K}]$	n_*	age [Myr]	[Fe/H]	$ED_{\text{min}} [\text{s}]$	α_B	α_{MK}	$\beta_2 [\text{yr}^{-1}]$	$\beta_B [\text{yr}^{-1}]$	$\beta_{MK} [\text{yr}^{-1}]$	tr_2	tr_B	tr_{MK}	
Pleiades	4000	4999	87	110	$125 \pm^{25}_{25}$	-0.02 ± 0.03	$2.3 \cdot 10^1$	1.68 ± 0.07	175.40 ± 3.06	26.23 ± 1.80	26.08 ± 1.74	0	0	0	
Pleiades	3000	3249	353	129	$125 \pm^{25}_{25}$	-0.02 ± 0.03	$9.1 \cdot 10^2$	2.26 ± 0.12	2.24 ± 0.12	1663.97 ± 8.43	16801.52 ± 1988.56	14323.95 ± 1675.01	0	0	0
Pleiades	3250	3499	168	185	$125 \pm^{25}_{25}$	-0.02 ± 0.03	$2.2 \cdot 10^2$	2.03 ± 0.09	2.02 ± 0.09	1250.16 ± 3.32	1524.74 ± 130.65	1437.66 ± 122.52	0	0	0
Pleiades	2500	2999	63	28	$125 \pm^{25}_{25}$	-0.02 ± 0.03	$2 \cdot 10^2$	1.40 ± 0.32	1.38 ± 0.26	732.64 ± 89.39	3.07 ± 0.97	2.55 ± 0.68	0	1	1
Pleiades	3750	3999	52	61	$125 \pm^{25}_{25}$	-0.02 ± 0.03	$4.6 \cdot 10^1$	1.86 ± 0.12	1.84 ± 0.11	337.15 ± 3.77	133.53 ± 15.57	118.85 ± 13.38	0	0	0
Pleiades	5000	5999	53	14	$125 \pm^{25}_{25}$	-0.02 ± 0.03	4.9	1.27 ± 0.25	1.32 ± 0.17	9.24 ± 1.16	0.13 ± 0.03	0.20 ± 0.04	1	1	1
Pleiades	3500	3749	50	47	$125 \pm^{25}_{25}$	-0.02 ± 0.03	$1.6 \cdot 10^2$	1.88 ± 0.11	1.84 ± 0.11	838.25 ± 8.01	338.29 ± 38.96	256.41 ± 28.27	0	0	0
M35	4000	4999	221	7	$149 \pm^{13}_{13}$	-0.21 ± 0.06	$5.2 \cdot 10^2$	-	1.34 ± 0.76	202.70 ± 21.23	-	0.26 ± 0.20	1	0	1
Rup 147	5000	5999	39	7	$2301 \pm^{380}_{257}$	0.08 ± 0.04	4.0	-	1.95 ± 0.30	3.07 ± 0.21	-	2.58 ± 0.79	0	0	0
Hyades	4000	4999	32	22	$665 \pm^{76}_{76}$	0.13 ± 0.01	4.4	-	1.13 ± 0.25	30.87 ± 8.30	-	0.05 ± 0.01	0	0	1
Hyades	3000	3249	56	14	$665 \pm^{70}_{70}$	0.13 ± 0.01	$9.8 \cdot 10^2$	1.87 ± 0.60	1.78 ± 0.48	1037.31 ± 28.99	316.11 ± 191.27	132.35 ± 63.88	0	1	1
Hyades	3250	3499	42	20	$665 \pm^{70}_{70}$	0.13 ± 0.01	$5.5 \cdot 10^2$	1.82 ± 0.37	1.77 ± 0.30	1281.92 ± 18.75	264.94 ± 97.28	156.31 ± 46.78	0	1	1
Hyades	3750	3999	5	21	$665 \pm^{70}_{70}$	0.13 ± 0.01	3.9	1.46 ± 0.29	1.49 ± 0.27	157.65 ± 8.25	8.37 ± 2.48	10.09 ± 2.71	0	1	1
Hyades	5000	5999	11	8	$665 \pm^{70}_{70}$	0.13 ± 0.01	$2.4 \cdot 10^1$	-	1.06 ± 0.28	182.82 ± 18.30	-	0.01 ± 0.00	1	0	1
Hyades	3500	3749	14	30	$665 \pm^{70}_{70}$	0.13 ± 0.01	6.5	-	1.14 ± 0.16	172.86 ± 33.54	-	0.18 ± 0.03	0	0	1

530 with field stars that systematically reduce the flaring rates. Applying our own restriction the M37 sample (Chang et al. 2016) leaves very few flares that hamper a statistical description of the distributions.

534 5.3. Division at 3000 K

535 The lowest T_{eff} bin at Pleiades age in our sample reflects the division between fully convective stars and those with a radiative core (Reid & Hawley 2005). At this age, the coolest dwarfs may still be accreting angular momentum on the PMS, instead of spinning down on the MS. We suggest that a regime change occurs around 120 Myr for stars with $T_{\text{eff}} = 2500 - 3250$ K. Below 3000 K, an analysis of 66 ZDI maps show that magnetic field configurations can be strong and dipolar or weak and tipolar (Morin et al. 2008; See et al. 2017). If these stars can be distinguished by age, this should be reflected in our age-resolved flaring activity. If the difference is not a function of age, we should see a similar bimodal distribution of very inactive and very active stars in the lowest mass bins. If the difference between the two configurations is a function of age, we should only see one type of stars with correspondingly similar behaviour in these T_{eff} bins.

536 The lowest mass bin appears underactive compared to the rest of the flaring-age- T_{eff} relation in the ED domain. Physical explanations for this peculiarity include: A different magnetic structure. A truncation of the power law that reflects the maximum active region can produce on these stars.

537 West et al. (2015) found that all M1-M4 dwarfs with rotation periods shorter than 26 days, and all M5-M8 dwarfs with periods shorter than 86 days show H α emission, indicating their magnetic activity.

538 Assuming a typical binary fraction for early and mid M dwarfs (Fischer & Marcy 1992), we can expect some of the flares on stars at $T_{\text{eff}} > 3000$ K to belong to unresolved binary companions with $T_{\text{eff}} < 3000$ K. A misattributed flare on an early M dwarf then will be assigned a too small ED , but still a correct $E_{Kp,\text{flare}}$ because the count ratios are equal to the L_{Kp} ratios.

539 5.4. Consistency of Hyades' and Praesepe's results

540 HRDs constructed in Gaia Collaboration et al. (2018a) indicate very similar ages for Hyades and Praesepe. We expect our results to reflect this similarity.

541 Are the samples comparable? Membership determination methods differ. Can we frame this as a statistical test, i.e. answer the question: What is the probability that the activity distributions for both clusters were drawn from the same underlying distribution for a given age and mass bin?

542 Metallicity is controlled for ([Fe/H](Praesepe) = 0.16, Netopil et al. 2016); ([Fe/H](Hyades) = 0.13, Netopil et al. 2016).

543 5.5. Consistency of Pleiades and M35 results

544 M35 is has subsolar metallicity, while Pleiades are roughly solar.

545 5.6. Jim's section(s)

546 Flaring activity function of mass and age – a gyrochronology analog?

547 Results in the context of Davenport et al. (2019): How well does the model fit if we have isochronal and not rotational ages for our stars?

Davenport et al. (2019) note a sample bias towards more active stars. Their models overpredicts the superflaring rate of the average Sun-like sample from Shibayama et al. (2013) and more resembles the rate for their most active sub-sample. Do we see the same effect in our OC sample? We should not. Our cluster memberships depend on activity.

548 5.7. Universality of α

549 Takin into account uncertainties and systematic errors resulting power law fitting methods, the power law exponent $\alpha \sim 2$ appears to be constant for all studies on flare statistics so far, irrespective of spectral type. A noteable exception are A stars in Kepler that follow a power law with $\alpha \sim 1$ that may indicate a different physical process (Yang & Liu 2019).

550 5.8. Deviations from single power law

551 Spots can survive on the stellar surface from a few days to nearly a year (Namekata et al. 2017; Davenport 2015). Namekata et al. (2017) find conceivable that spots evolve on timescale shorter than the estimated lifetimes. Complex spot geometry is correlated with the strongest X-class flares on the Sun (Toriumi et al. 2017; Sammis et al. 2000). This support the idea that flares are associated with the presence of certain types of starspots, or more generally, certain types of active regions. Since we can reasonable expect that there is a maximum flare energy a spot can produce, the underlying power law relation must break a some ED_{max} . We tested a possible truncation of our FFDs, but find no conclusive evidence for it in any FFD with > 50 data points. As we stack multiple targets, each potentially with multiple, evolving spots of various sizes on their surfaces, into one FFD at a time, we might observe a deviation but no truncation. A different explanation is simply that we do not sample the maximum energies, as extremely high relative fluxes have been observed in the past (Paudel et al. 2018; Jackman et al. 2019; Schmidt et al. 2016).

6. Summary and Conclusions

552 Is there or will be there more data available to further extend the sample?

553 Acknowledgements. This work made use of the `gaia-kepler.fun` crossmatch database created by Megan Bedell. Kepler-affiliated tools were used in the process: `lightkurve`, `K2SC`, `AltaiPony`. Also: `numpy`, `pandas`, `astroML`, `astropy`, `specmatch-emp`, `bokeh` (Bokeh Development Team 2019)... TOPCAT: This research made use of the cross-match service provided by CDS, Strasbourg. This work has made use of data from the European Space Agency (ESA) mission `Gaia` (<https://www.cosmos.esa.int/gaia>), processed by the `Gaia` Data Processing and Analysis Consortium (DPAC, <https://www.cosmos.esa.int/web/gaia/dpac/consortium>). Funding for the DPAC has been provided by national institutions, in particular the institutions participating in the `Gaia` Multilateral Agreement. If you have used `Gaia` DR2 data in your research, please cite both the `Gaia` mission paper and the `Gaia` DR2 release paper: Gaia Collaboration et al. (2016): Description of the `Gaia` mission (spacecraft, instruments, survey and measurement principles, and operations), Gaia Collaboration et al. (2018b): Summary of the contents and survey properties.

References

- Aarnio, A. N., Matt, S. P., & Stassun, K. G. 2012, ApJ, 760, 9
- Aarnio, A. N., Stassun, K. G., Hughes, W. J., & McGregor, S. L. 2011, Sol. Phys., 268, 195
- Aigrain, S., Parviainen, H., & Pope, B. J. S. 2016, MNRAS, 459, 2408
- Alvarado-Gómez, J. D., Drake, J. J., Cohen, O., Moschou, S. P., & Garraffo, C. 2018, ApJ, 862, 93

- 643 Andrae, R., Fouesneau, M., Creevey, O., et al. 2018, A&A, 616, A8 723
 644 Barentsen, G., Hedges, C., Saunders, N., et al. 2018, arXiv e-prints 724
 645 arXiv:1810.12554 725
 646 Barnes, S. A. 2003, ApJ, 586, 464 726
 647 Bauke, H. 2007, European Physical Journal B, 58, 167 727
 648 Bessell, M. S. & Brett, J. M. 1988, Publications of the Astronomical Society of the Pacific, 100, 1134 728
 649 Bochanski, J. J., Hawley, S. L., Covey, K. R., et al. 2010, AJ, 139, 2679 729
 650 Bochanski, J. J., West, A. A., Hawley, S. L., & Covey, K. R. 2007, AJ, 133, 534 730
 651 Bokeh Development Team. 2019, Bokeh: Python library for interactive visualization 731
 652 Bouy, H., Bertin, E., Barrado, D., et al. 2015, Astronomy and Astrophysics, 5734 733
 653 A120 735
 654 Boyajian, T. S., von Braun, K., van Belle, G., et al. 2013, The Astrophysical Journal, 736 736
 655 771, 40 737
 656 Burgasser, A. J., Cruz, K. L., Cushing, M., et al. 2010, ApJ, 710, 1142 738
 657 Burgasser, A. J., Liu, M. C., Ireland, M. J., Cruz, K. L., & Dupuy, T. J. 2008, ApJ, 681, 579 739
 658 Burgasser, A. J., Looper, D. L., Kirkpatrick, J. D., & Liu, M. C. 2007, ApJ, 658 740
 659 Candelaresi, S., Hillier, A., Maehara, H., Brandenburg, A., & Shibata, K. 2014, ApJ, 792, 67 741
 660 Cantat-Gaudin, T., Jordi, C., Vallenari, A., et al. 2018, A&A, 618, A93 742
 661 Carpenter, J. M. 2001, The Astronomical Journal, 121, 2851 743
 662 Chambers, K. C., Magnier, E. A., Metcalfe, N., et al. 2016, ArXiv e-prints 748
 663 [arXiv:1612.05560] 749
 664 Chang, S.-W., Byun, Y.-I., & Hartman, J. D. 2015, ApJ, 814, 35 750
 665 Chang, S. W., Byun, Y. I., & Hartman, J. D. 2016, VizieR Online Data Catalog, 751
 666 7/ApJ/814/35 752
 667 Clarke, R. W., Davenport, J. R. A., Covey, K. R., & Baranec, C. 2018, ApJ, 853 753
 668 Cruz, K. L., Burgasser, A. J., Reid, I. N., & Liebert, J. 2004, ApJ, 604, L61 755
 669 Cruz, K. L., Reid, I. N., Liebert, J., Kirkpatrick, J. D., & Lowrance, P. J. 2009, AJ, 126, 2421 756
 670 Curtis, J. L., Wolfgang, A., Wright, J. T., Brewer, J. M., & Johnson, J. A. 2009, AJ, 145, 134 758
 671 Davenport, J. 2015, PhD thesis, University of Washington 760
 672 Davenport, J. R. A., Covey, K. R., Clarke, R. W., et al. 2019, ApJ, 871, 241 761
 673 Davenport, J. R. A., Hawley, S. L., Hebb, L., et al. 2014, ApJ, 797, 122 762
 674 Doi, M., Tanaka, M., Fukugita, M., et al. 2010, AJ, 139, 1628 763
 675 Doorsselaere, T. V., Sharati, H., & Debosscher, J. 2017, ApJS, 232, 26 764
 676 Douglas, S. T., Agüeros, M. A., Covey, K. R., et al. 2014, ApJ, 795, 161 765
 677 Douglas, S. T., Agüeros, M. A., Covey, K. R., et al. 2016, ApJ, 822, 47 766
 678 Douglas, S. T., Agüeros, M. A., Covey, K. R., & Kraus, A. 2017, ApJ, 842, 8267 767
 679 Drake, J. J., Cohen, O., Yashiro, S., & Gopalswamy, N. 2013, ApJ, 764, 170768 768
 680 Filippazzo, J. C., Rice, E. L., Faherty, J., et al. 2015, ApJ, 810, 158 769
 681 Finkbeiner, D. P., Schlafly, E. F., Schlegel, D. J., et al. 2016, ApJ, 822, 66 770
 682 Fischer, D. A., & Marcy, G. W. 1992, ApJ, 396, 178 771
 683 Froning, C. S., Kowalski, A., France, K., et al. 2019, ApJ, 871, L26 772
 684 Gaia Collaboration, Babusiaux, C., van Leeuwen, F., et al. 2018a, A&A, 617, A10 773
 685 Gaia Collaboration, Brown, A. G. A., Vallenari, A., et al. 2018b, A&A, 616, 774
 686 Gao, X. 2018, ApJ, 869, 9 775
 687 Gao, X. 2018, The Astrophysical Journal, 869, 9 776
 688 Gonzalez, G. 2016, MNRAS, 459, 1060 777
 689 Green, G. M., Schlafly, E. F., Finkbeiner, D., et al. 2018, MNRAS, 478, 651 780
 690 Green, G. M., Schlafly, E. F., Zucker, C., Speagle, J. S., & Finkbeiner, D. 2019, arXiv e-prints, arXiv:1905.02734 781
 691 Hawley, S. L. & Fisher, G. H. 1992, ApJS, 78, 565 782
 692 Hilton, E. J., West, A. A., Hawley, S. L., & Kowalski, A. F. 2010, AJ, 140, 1400 783
 693 Howard, W. S., Corbett, H., Law, N. M., et al. 2019a, ApJ, 881, 9 784
 694 Howard, W. S., Corbett, H., Law, N. M., et al. 2019b, arXiv e-prints, arXiv:1907.10735 785
 695 Howell, S. B., Sobeck, C., Haas, M., et al. 2014, PASP, 126, 398 786
 696 Hunt-Walker, N. M., Hilton, E. J., Kowalski, A. F., Hawley, S. L., & Matthews, J. M. 2012, PASP, 124, 545 787
 697 Ilin, E., Schmidt, S. J., Davenport, J. R. A., & Strassmeier, K. G. 2019, A&A, 622, A133 788
 698 Jackman, J. A. G., Wheatley, P. J., Bayliss, D., et al. 2019, arXiv e-prints, arXiv:1902.00900 789
 699 Karoff, C. 2016, Nature Communications, 7, 11058
 700 Kerr, G. S. & Fletcher, L. 2014, ApJ, 783, 98
 701 Kirkpatrick, J. D.,Looper, D. L.,Burgasser, A. J.,et al. 2010, ApJS, 190, 100
 702 Kleint, L.,Heinzel, P.,Judge, P.,& Krucker, S. 2016, ApJ, 816, 88
 703 Koch, D. G., Borucki, W. J., Basri, G., et al. 2010, ApJ, 713, L79
 704 Kovács, G., Bakos, G., & Noyes, R. W. 2005, MNRAS, 356, 557
 705 Kowalski, A. F., Hawley, S. L., Wisniewski, J. P., et al. 2013, ApJS, 207, 15
 706 Kretzschmar, M. 2011, A&A, 530, A84
 707 Lecavelier des Etangs, A., Bourrier, V., Wheatley, P. J., et al. 2012, A&A, 543, L4
 708 Loyd, R. O. P., France, K., Youngblood, A., et al. 2018, ApJ, 867, 71
 709 Luger, R., Kruse, E., Foreman-Mackey, D., Agol, E., & Saunders, N. 2018, AJ, 156, 99
 710 Lurie, J. C., Davenport, J. R. A., Hawley, S. L., et al. 2015, ApJ, 800, 95
 711 Mann, A. W., Feiden, G. A., Gaidos, E., Boyajian, T., & von Braun, K. 2015, ApJ, 804, 64
 712 Mann, A. W., Feiden, G. A., Gaidos, E., Boyajian, T., & von Braun, K. 2016, The Astrophysical Journal, 819, 87
 713 Maschberger, T. & Kroupa, P. 2009, MNRAS, 395, 931
 714 Mondrik, N., Newton, E., Charbonneau, D., & Irwin, J. 2019, ApJ, 870, 10
 715 Morin, J., Donati, J. F., Petit, P., et al. 2008, MNRAS, 390, 567
 716 Namekata, K., Sakaue, T., Watanabe, K., et al. 2017, ApJ, 851, 91
 717 Nardiello, D., Libralato, M., Bedin, L. R., et al. 2016, MNRAS, 463, 1831
 718 Olivares, J., Bouy, H., Sarro, L. M., et al. 2019, A&A, 625, A115
 719 Olivares, J., Sarro, L. M., Moraux, E., et al. 2018, A&A, 617, A15
 720 Paudel, R. R., Gizis, J. E., Mullan, D. J., et al. 2018, ApJ, 861, 76
 721 Pecaut, M. J. & Mamajek, E. E. 2013, ApJS, 208, 9
 722 Priest, E. & Forbes, T. 2002, A&A Rev., 10, 313
 723 Rayner, J. T., Cushing, M. C., & Vacca, W. D. 2009, ApJS, 185, 289
 724 Rebull, L., Stauffer, J., Bouvier, J., et al. 2016a, Astronomical Journal, 152, 113, bibtext: 2016AJ....152..113R bibtext[eid=113;adsurl=https://ui.adsabs.harvard.edu/abs/2016AJ....152..113R;adsnote=Provided by the SAO/NASA Astrophysics Data System]
 725 Rebull, L. M., Stauffer, J. R., Bouvier, J., et al. 2016b, AJ, 152, 113
 726 Rebull, L. M., Stauffer, J. R., Hillenbrand, L. A., et al. 2017, ApJ, 839, 92
 727 Reid, I. N. & Hawley, S. L. 2005, New Light on Dark Stars: Red Dwarfs, Low-Mass Stars, Brown Dwarfs, 2nd edn., Springer-Praxis books in astronomy and astrophysics (Berlin ; New York : Chichester, UK: Springer ; Praxis)
 728 Reino, S., de Bruijne, J., Zari, E., d'Antona, F., & Ventura, P. 2018, MNRAS, 477, 3197
 729 Sammis, I., Tang, F., & Zirin, H. 2000, ApJ, 540, 583
 730 Schmidt, S. J. 2014, Mem. Soc. Astron. Italiana, 85, 741
 731 Schmidt, S. J., Hawley, S. L., West, A. A., et al. 2015, AJ, 149, 158
 732 Schmidt, S. J., Shappee, B. J., Gagné, J., et al. 2016, ApJ, 828, L22
 733 Schmidt, S. J., West, A. A., Bochanski, J. J., Hawley, S. L., & Kielty, C. 2014, PASP, 126, 642
 734 Schmidt, S. J., West, A. A., Hawley, S. L., & Pineda, J. S. 2010, AJ, 139, 1808
 735 See, V., Jardine, M., Vidotto, A. A., et al. 2017, MNRAS, 466, 1542
 736 Shibayama, T., Maehara, H., Notsu, S., et al. 2013, The Astrophysical Journal Supplement Series, 209, 5
 737 Shibayama, T., Maehara, H., Notsu, S., et al. 2013, ApJS, 209, 5
 738 Skrutskie, M. F., Cutri, R. M., Stiening, R., et al. 2006, AJ, 131, 1163
 739 Soares-Furtado, M., Hartman, J. D., Bakos, G. Á., et al. 2017, Publications of the Astronomical Society of the Pacific, 129, 044501
 740 Tilley, M. A., Segura, A., Meadows, V., Hawley, S., & Davenport, J. 2019, Astrobiology, 19, 64
 741 Toriumi, S., Schrijver, C. J., Harra, L. K., Hudson, H., & Nagashima, K. 2017, ApJ, 834, 56
 742 Van Cleve, J. E., Howell, S. B., Smith, J. C., et al. 2016, PASP, 128, 075002
 743 Vanderburg, A. & Johnson, J. A. 2014, Publications of the Astronomical Society of the Pacific, 126, 948
 744 Vanderplas, J., Connolly, A., Ivezić, Ž., & Gray, A. 2012, in Conference on Intelligent Data Understanding (CIDU), 47–54
 745 Vinícius, Z., Barentsen, G., Hedges, C., Gully-Santiago, M., & Cody, A. M. 2018 Walkowicz, L. M., Basri, G., Batalha, N., et al. 2011, AJ, 141, 50
 746 Watanabe, K., Shimizu, T., Masuda, S., Ichimoto, K., & Ohno, M. 2013, ApJ, 776, 123
 747 West, A. A., Morgan, D. P., Bochanski, J. J., et al. 2011, AJ, 141, 97
 748 West, A. A., Weisenburger, K. L., Irwin, J., et al. 2015, ApJ, 812, 3
 749 Wheatland, M. S. 2004, ApJ, 609, 1134
 750 Yang, H. & Liu, J. 2019, ApJS, 241, 29
 751 Yang, H., Liu, J., Gao, Q., et al. 2017, ApJ, 849, 36
 752 Yang, H., Liu, J., Qiao, E., et al. 2018, ApJ, 859, 87
 753 Yee, S. W., Petigura, E. A., & von Braun, K. 2017, ApJ, 836, 77

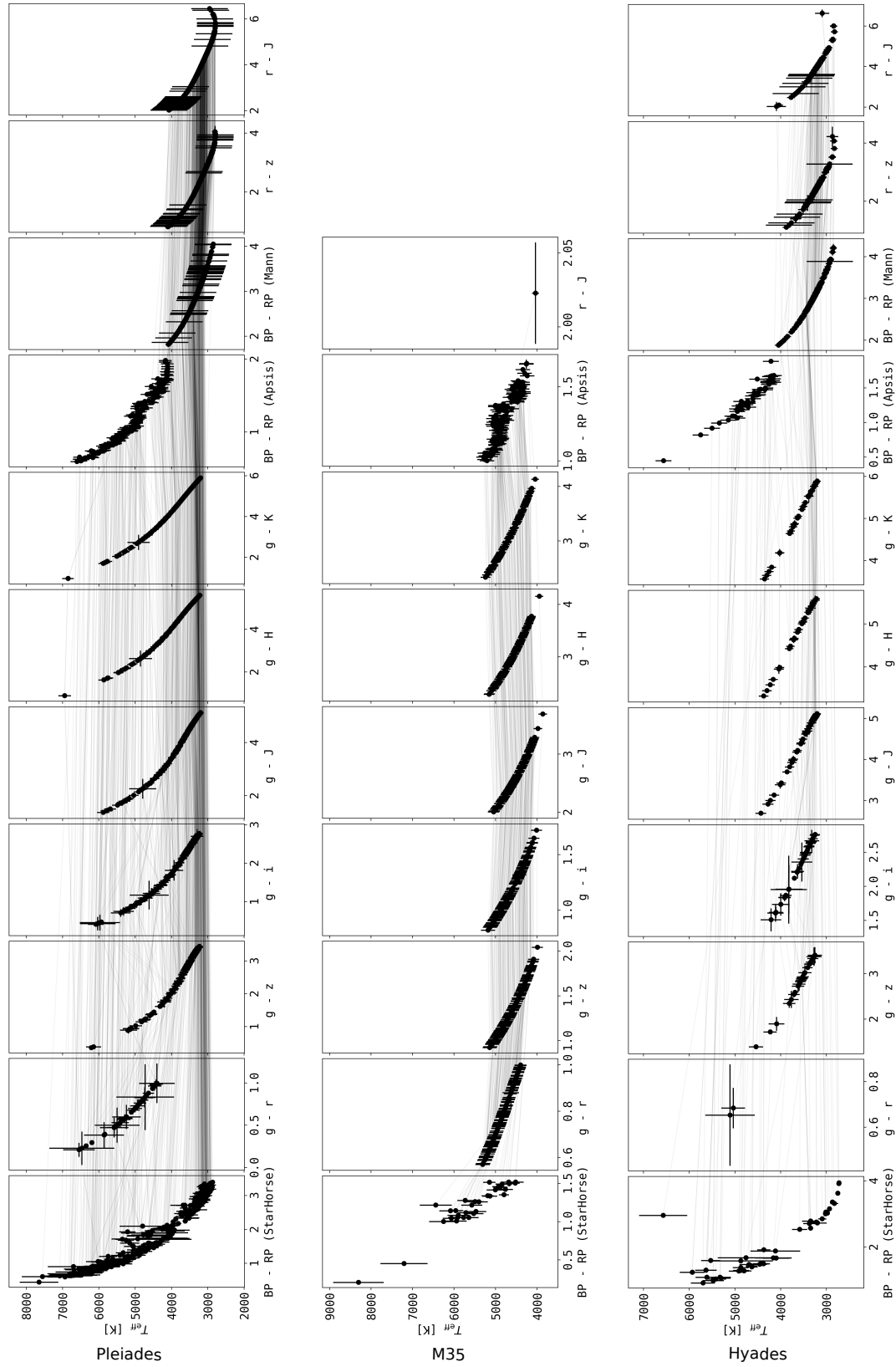


Fig. 2. Color-temperature relations for Pleiades, M35, and Hyades.

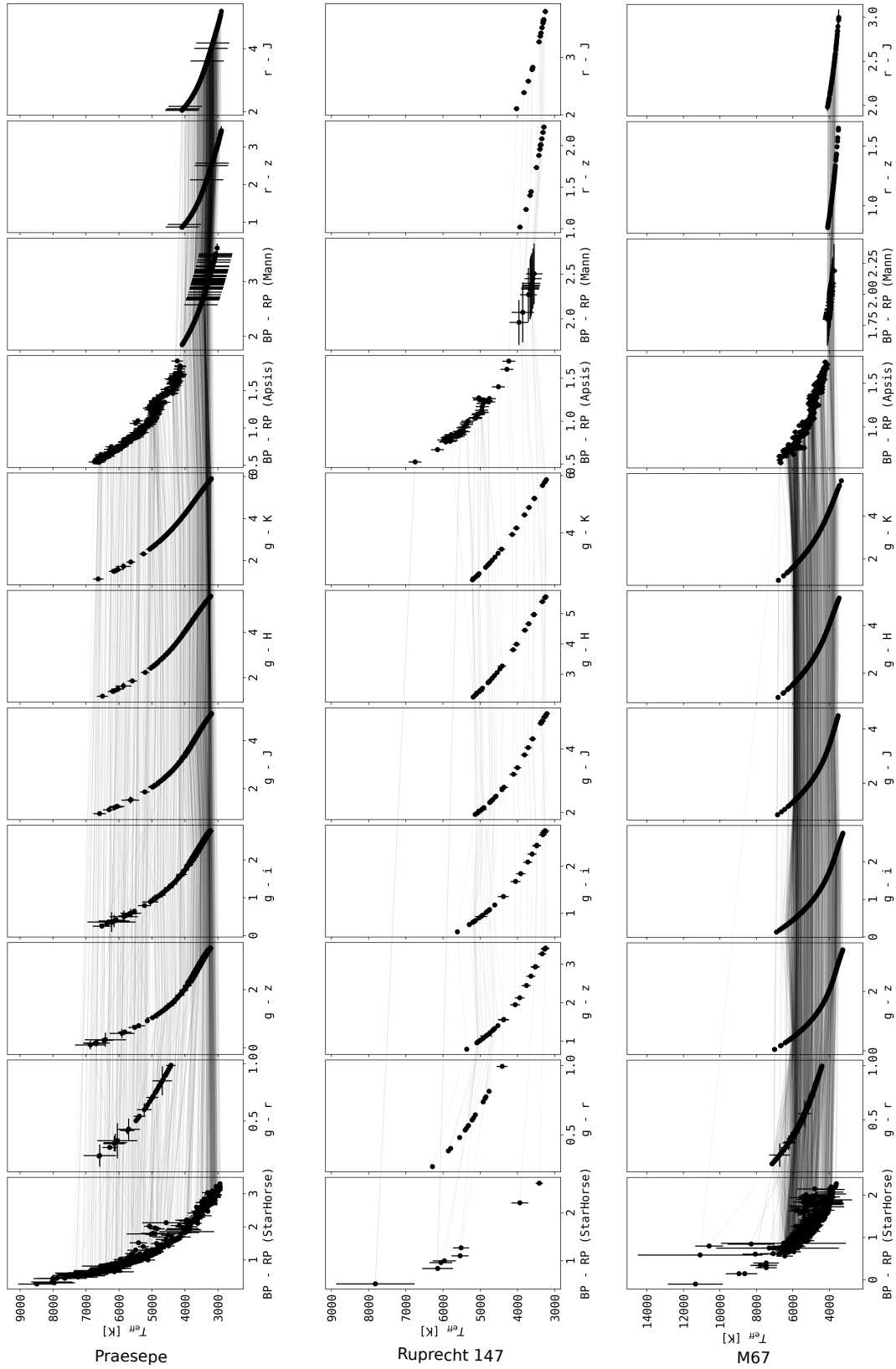


Fig. 3. Color-temperature relations for Praesepe, Ruprecht 147, and M67. Description as in Fig. 2.

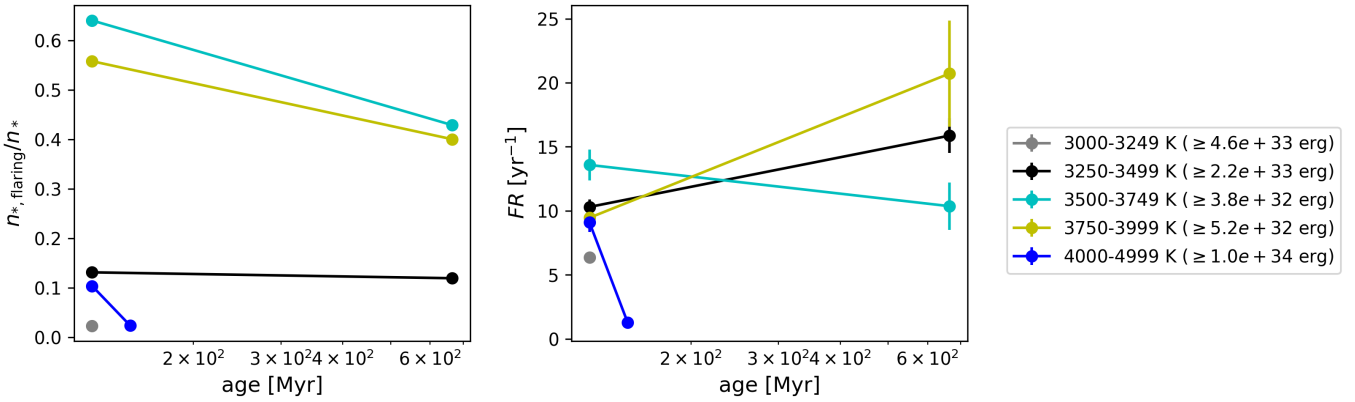


Fig. 4. Flaring activity in energy distributions. Left panel: Flaring fraction n_{flaring}/n_* . Right panel: Flaring rate FR . See Fig. 5 for details on the overall figure layout.

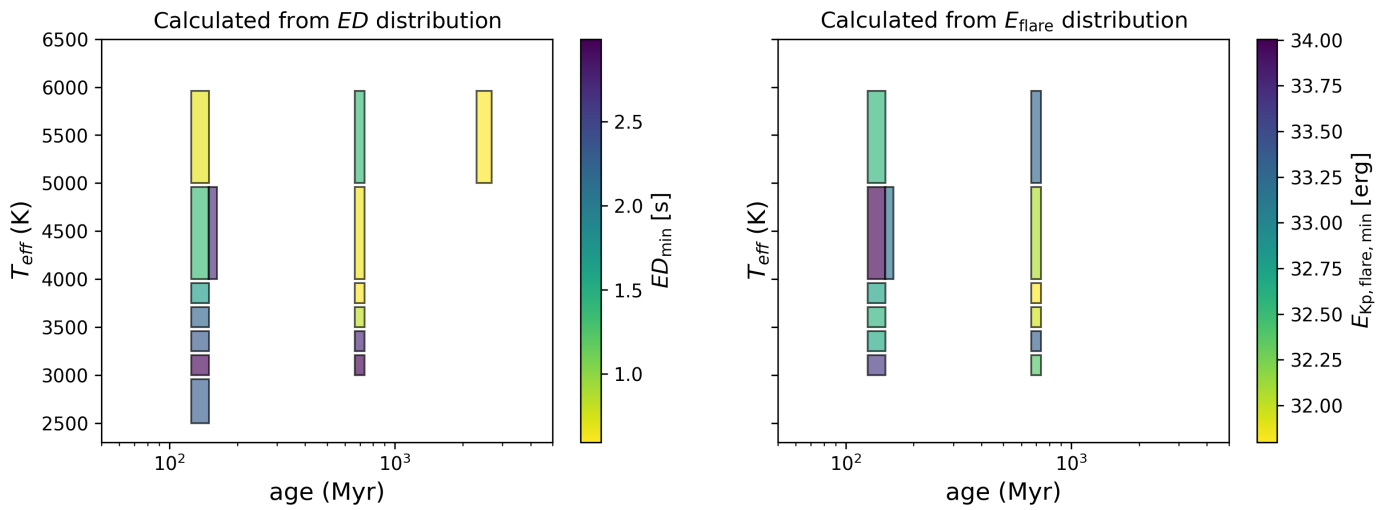


Fig. 5. E_{flare} and ED detection thresholds as a function of stellar age and T_{eff} . The rectangles' widths on the age axis reflect the uncertainty on the cluster ages found in the literature. The rectangles' widths on the T_{eff} axis encompass the temperature bins over which the thresholds were averaged.

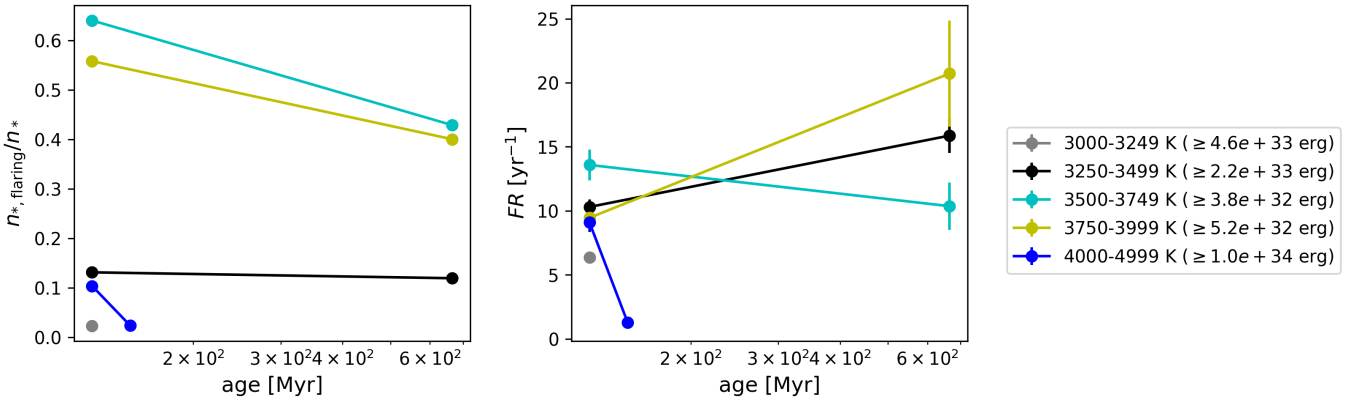


Fig. 6. Flaring activity in energy distributions. Left panel: Flaring fraction n_{flaring}/n_* . Right panel: Flaring rate FR . See Fig. 5 for details on the overall figure layout.

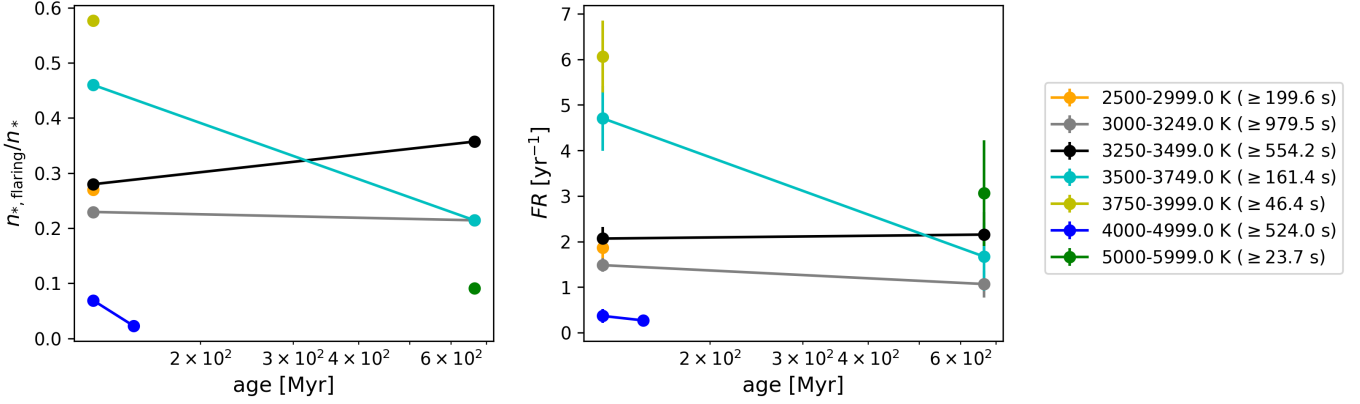


Fig. 7. Flaring activity in *ED* distributions. Left panel: Flaring fraction n_{flaring}/n^* . Right panel: Flaring rate FR . See Fig. ?? for details on the overall figure layout.

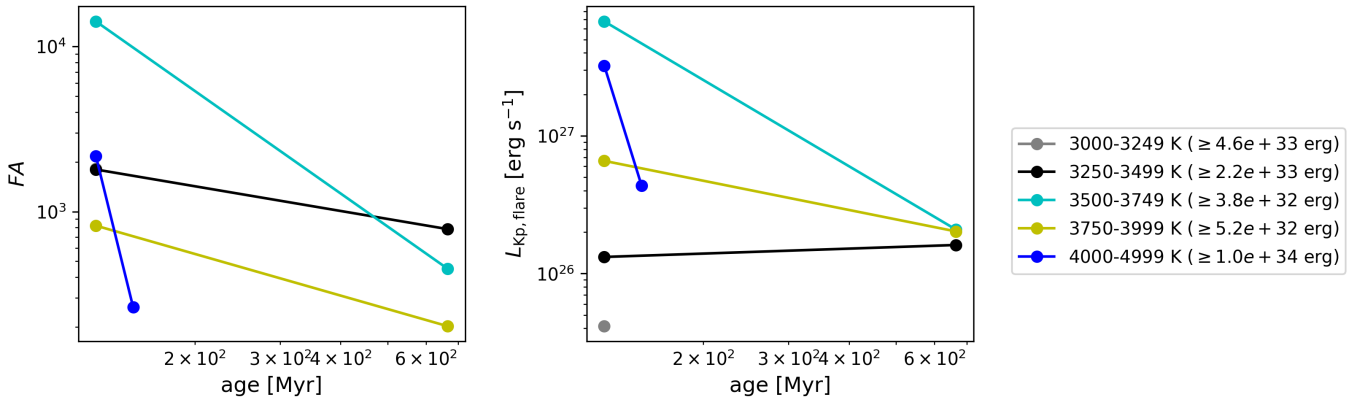


Fig. 8. Energy released in flares. Left panel: Energy released in flares relative to quiescent stellar luminosity FA . Right panel: Average flaring luminosity released in the Kepler band $L_{\text{Kp,flare}}$.

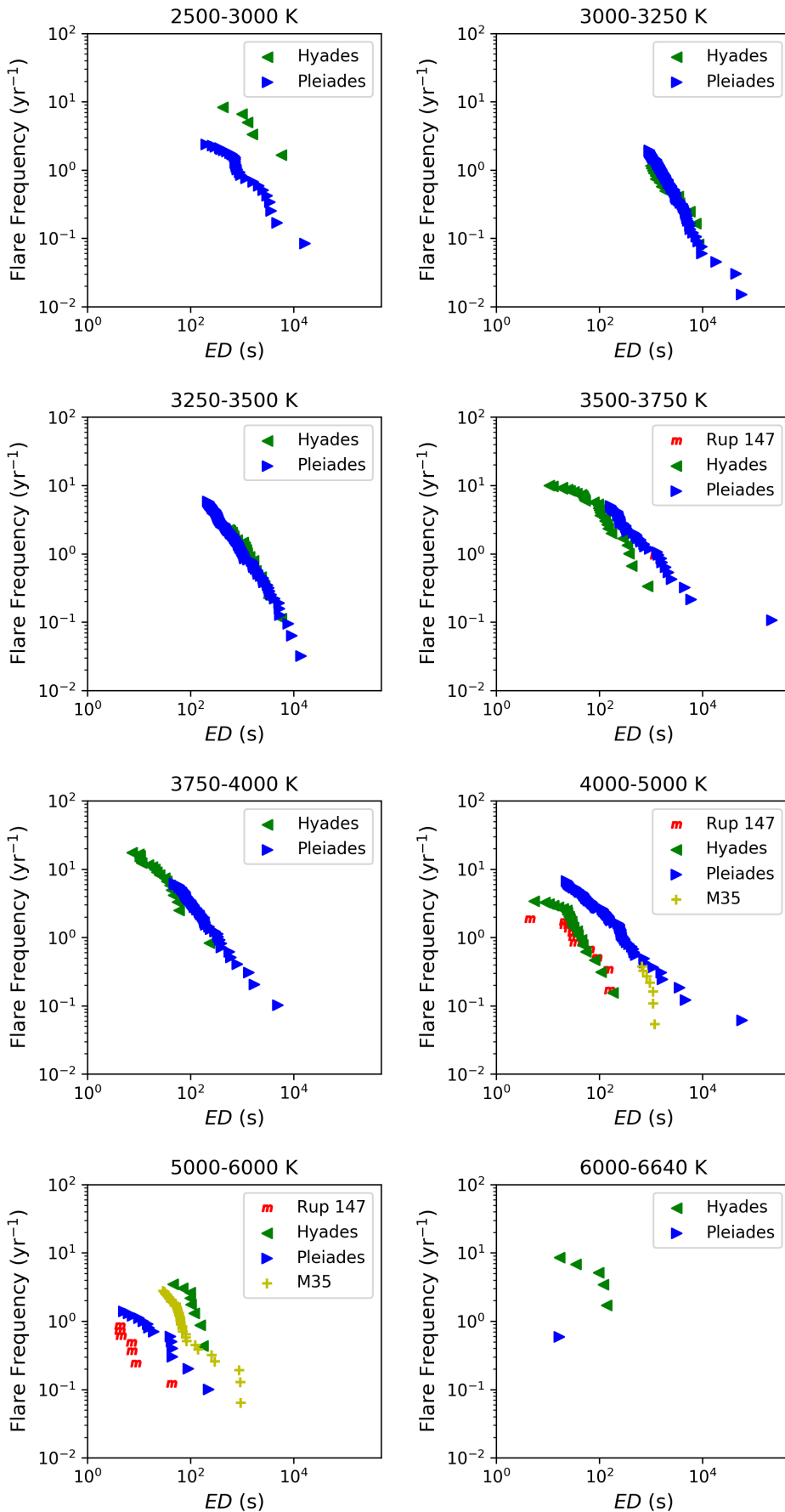


Fig. 9. Cumulative flare frequency distributions (FFDs) of equivalent durations (ED). In each panel, every distribution belongs to one cluster. The panels are binned by T_{eff} .

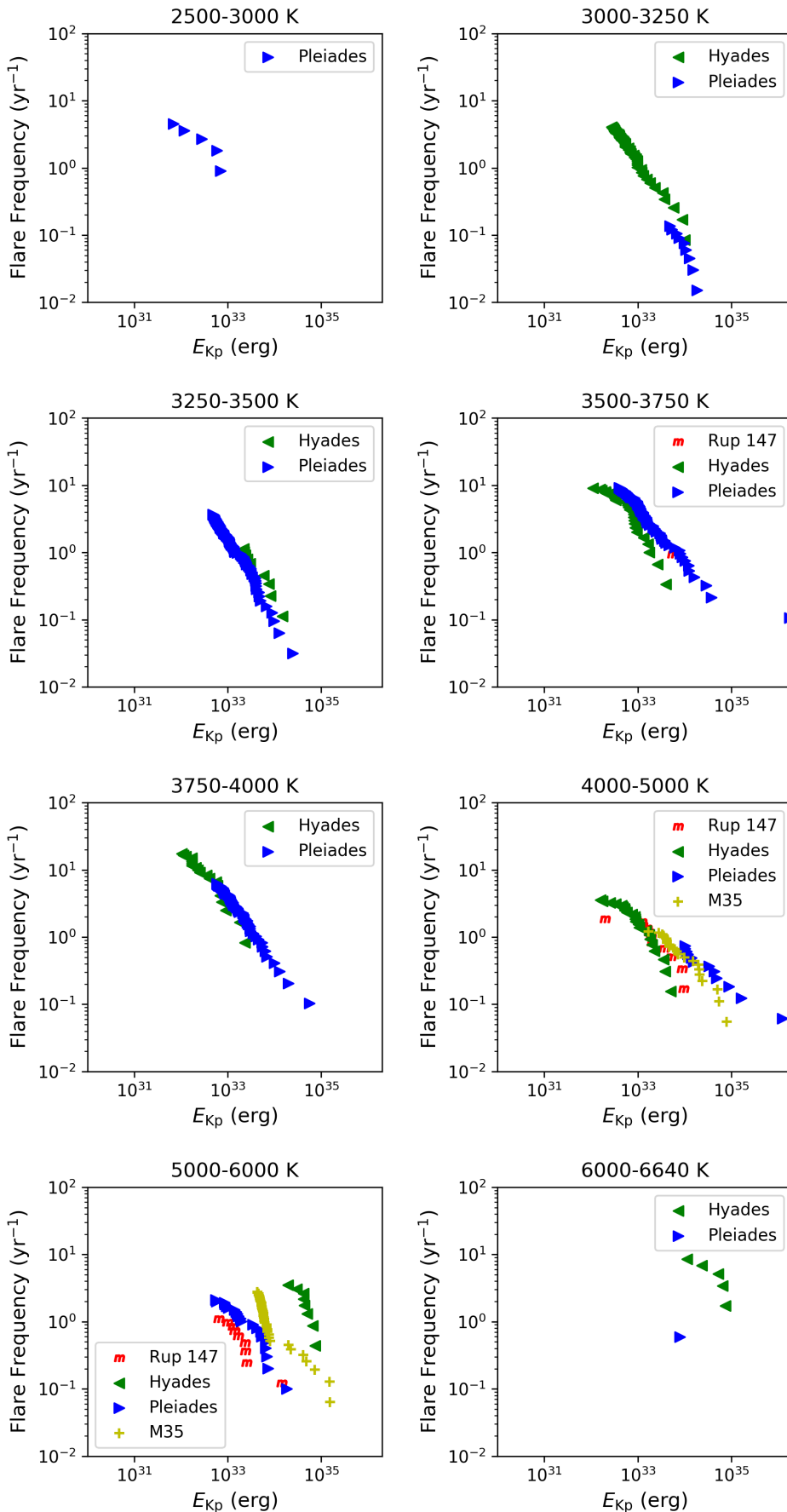


Fig. 10. Same as Fig. 9, but of Kepler flare energies $E_{Kp,\text{flare}}$.

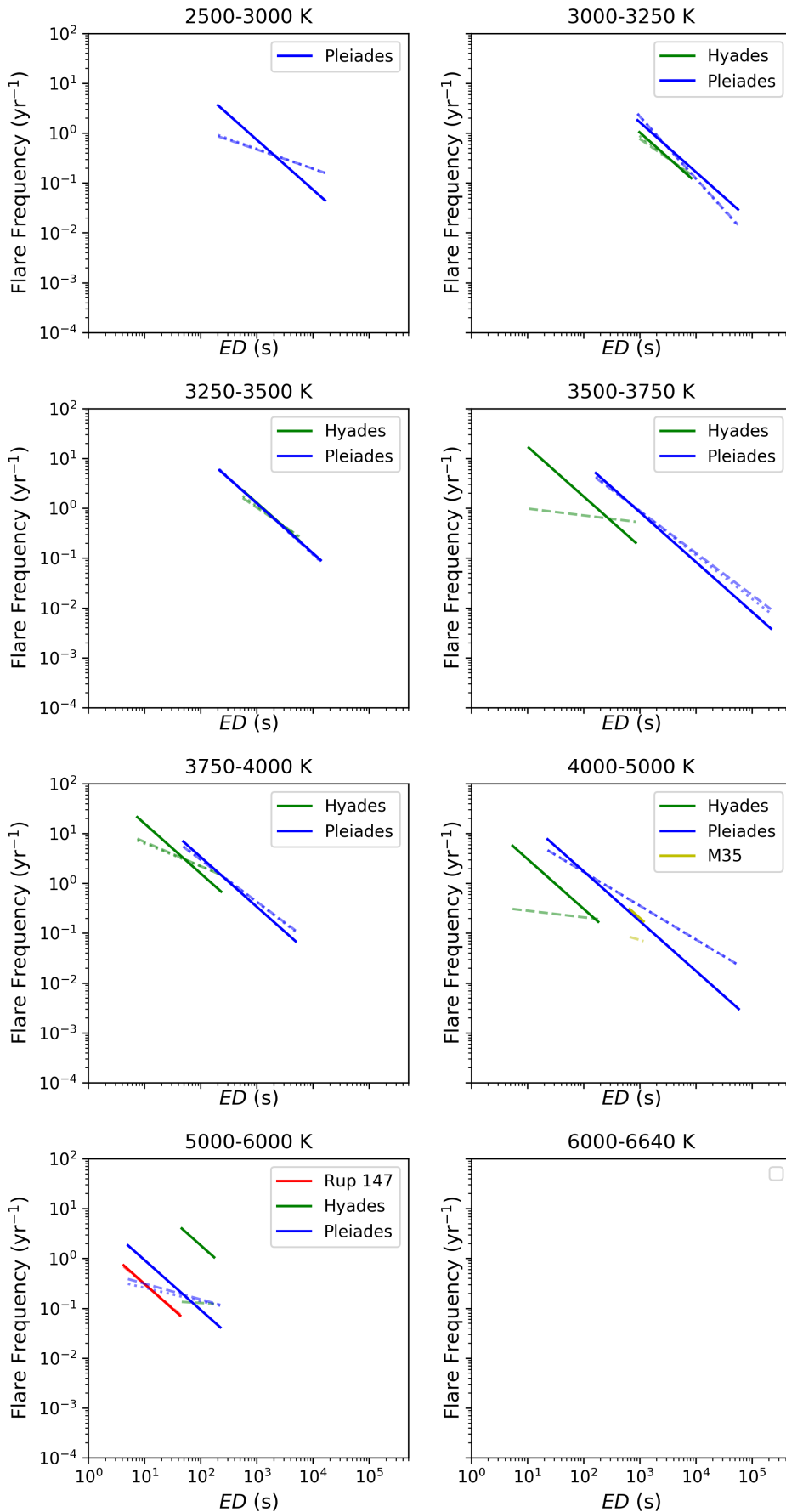


Fig. 11. Power law fits to the FFDs of ED in Fig. 9. Bold line: a power law with $\alpha = 2$. Dashed line: best fit parameters were determined following Maschberger & Kroupa (2009) (see Sec. XX). Dotted line: best fit parameters were determined following Bauke (2007) (see Sec. XX)

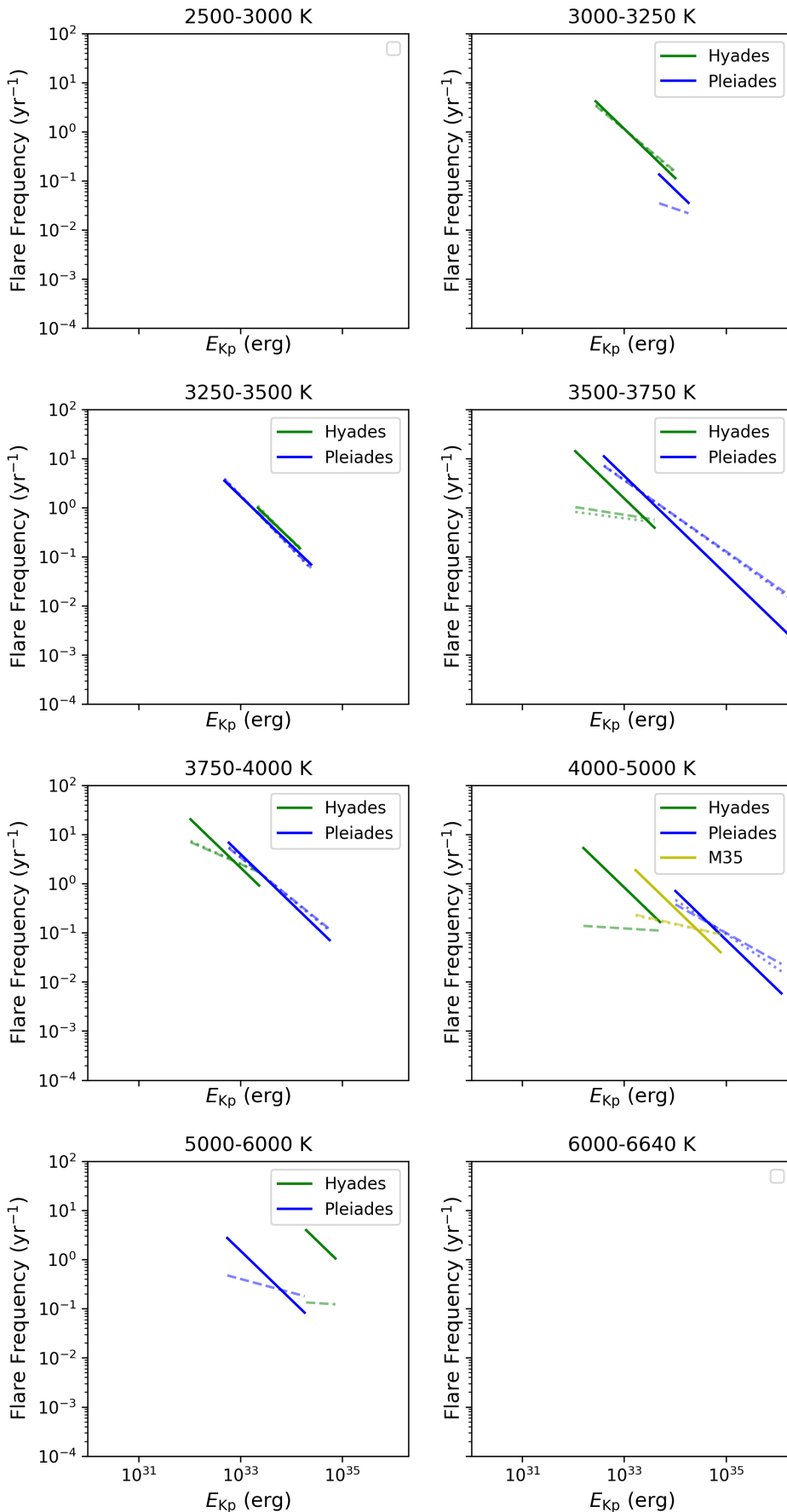


Fig. 12. Power law fits to the FFDs of $E_{\text{Kp,flare}}$ in Fig. 9. See Fig. 11 for details.

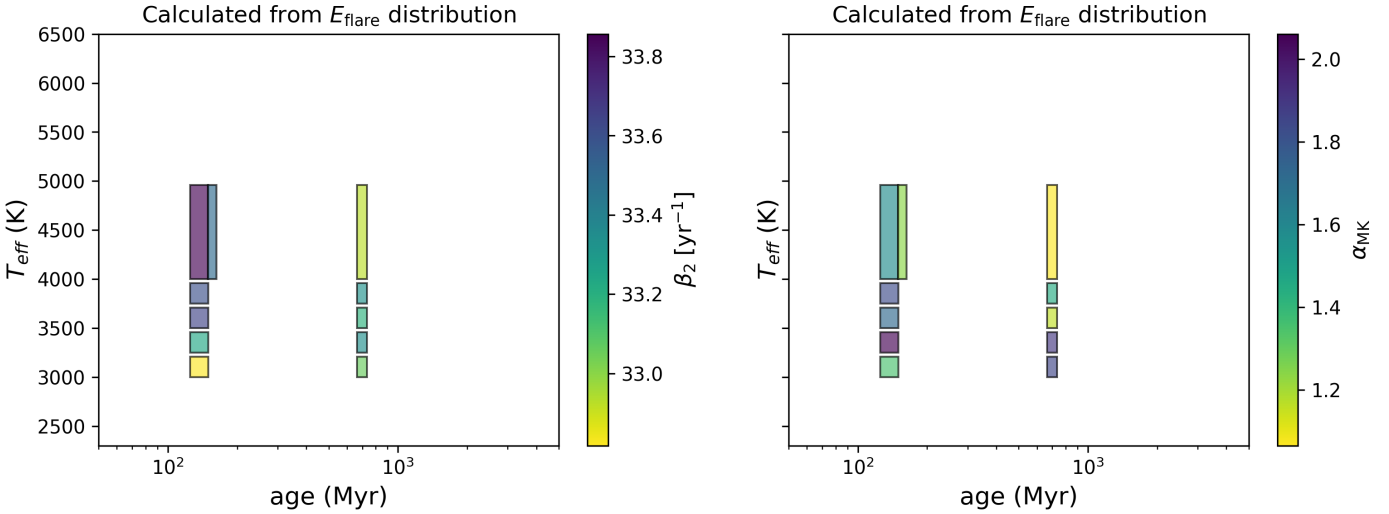


Fig. 13. Power law fit parameters in energy distributions. Left panel: Power law intercept β_2 . Right panel: Power law exponent α_{MK} , fitting procedure follows Mascherger and Kroupa (2009). See Fig. 5 for details on the overall figure layout.

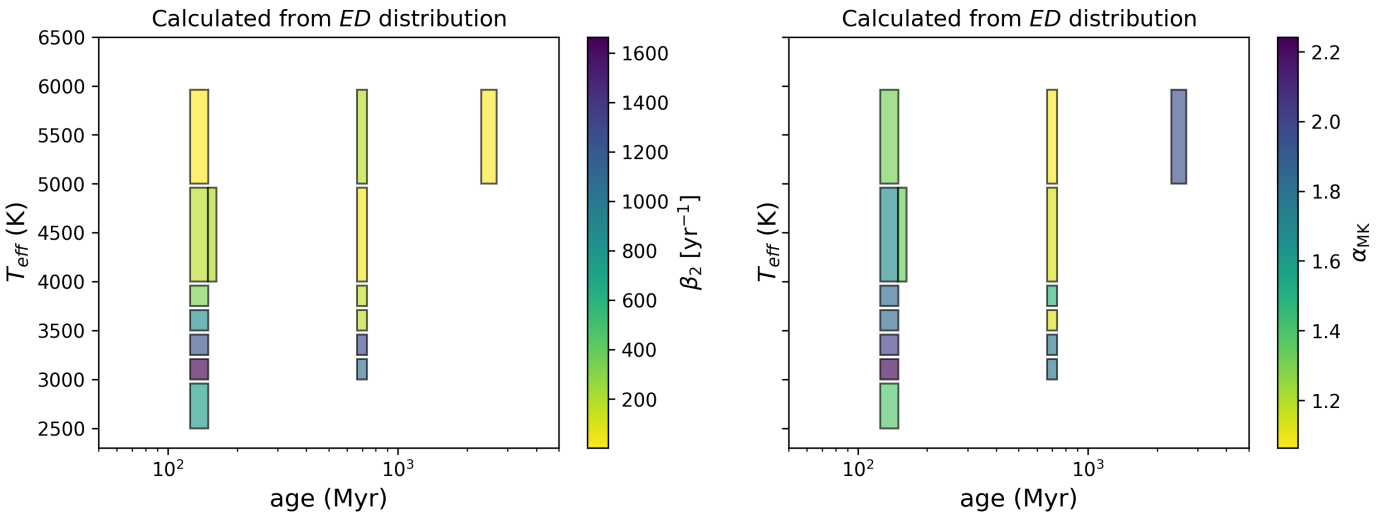


Fig. 14. Power law fit parameters in ED distributions. Left panel: Power law intercept β_2 . Right panel: Power law exponent α_{MK} , fitting procedure follows Mascherger and Kroupa (2009). See Fig. 5 for details on the overall figure layout.

790 Appendix A: Membership probabilities

791 To match catalogs on RA and declination we used `astroML.crossmatch` tool for Python (Vanderplas et al. 2013).
 792 For the studies with classifiers we assigned membership probabilities as follows. In Gonzalez (2016):
 793

$$\begin{aligned} p(M(\text{member})) &= 0.9, \\ p(BM(\text{binary member})) &= 0.9, \\ p(N(\text{non-member})) &= 0.1, \\ p(SN(\text{single non-member})) &= 0.1, \\ p(BN(\text{binary non-member})) &= 0.1, \\ p(U(\text{unknown member})) &= 0.5. \end{aligned}$$

795 In Curtis et al. (2013):

$$\begin{aligned} p(Y(\text{highest confidence member})) &= 0.9, \\ p(P(\text{possible/probable member})) &= 0.7, \\ p(N(\text{not likely/non-member})) &= 0.7, \\ p(B(\text{photometry consistent with blue stragglers})) &= 0.0. \end{aligned}$$

796 In Rebull et al. (2017):

$$\begin{aligned} p((\text{best})) &= 0.9, \\ p((\text{ok})) &= 0.6, \\ p((\text{else})) &= 0.1. \end{aligned}$$

797 Members from Rebull et al. (2016a); Douglas et al. (2017); and
 798 Gaia Collaboration et al. (2018a) were assigned $p = 0.9$ if they
 799 appeared in the final catalog.
 800 Table A.1 gives an overview over different membership catalogues.
 801 Figure A.1 shows membership probability histograms of the final sample broken down by membership source. Detailed instructions on how to reproduce the final sample of members in each cluster, and corresponding tables, Python scripts, and Jupyter notebooks can be found online⁵

806 Appendix B: Cluster parameters

807 Appendix C: Broadband photometry: quality cuts 808 and conversions

809 We required `flux/flux_error` ≥ 10 for Gaia G, BP, and RP
 810 bands. We require that the 2MASS measurements for J, H, and
 811 K to be "A". "A" means that measurements had $S/N > 10$ and
 812 $\sigma < 0.11$. For PanSTARRS photometry, we required that the
 813 QF_OBJ_GOOD quality filter flag was set.
 814 SDSS and PS1 *ugrizy* bands are similar but not identical, but can
 815 be converted using Table 2 in Finkbeiner et al. (2016).

816 Appendix D: Pixel saturation

817 Resolve different levels of pixel saturation (>1 , >10) and they contribute to the deviations from the single power law at
 818 the highest energies.
 819

⁵ <https://github.com/ekaterinailin/flares-in-clusters-with-k2-ii>

820 Appendix E: Solar system objects

821 Solar system objects (SSOs) produce brightness excursions in
 822 K2 light curves that can closely resemble flare signatures. Often,
 823 they can be distinguished by their symmetric rise and decay
 824 shape as contrasted with the typical fast-rise gradual decay flare
 825 shape (Davenport et al. 2014). M. H. Christiansen and colleagues
 826 developed a routine called SkyBoT that matches positions and
 827 times to passages of SSOs listed in YYY. RA, declination, start,
 828 stop, and mid epochs of flares in BKJD are the input parameters.
 829 We excluded all flare candidates that occurred within X minutes
 830 of a SSO passage at the star's position. This procedure removed
 831 ZZ% of all flare candidates. In the case of high energy flares, we
 832 confirmed the passage by manually inspecting the pixel file with
 833 the `lightkurve interact` function for TargetPixelFiles.

834 Appendix F: Universality of power law exponent α

835 We compiled a exhaustive (?) table of previous work where
 836 power laws were fitted to FFDs using different methods. Table
 837 F.1 lists the overview. While particular studies consistently find
 838 values above or below $\alpha \approx 2$, the comparison of different studies
 839 points towards unresolved systematic errors in all these studies.

840 Appendix G: Expanding the likelihood

The rate λ_2 of flares with energies larger than S_2 is given in Wheatland (2004) as

$$\lambda_2 = \lambda_1 \cdot \left(\frac{S_1}{S_2} \right)^{\alpha-1}. \quad (\text{G.1})$$

S_1 denotes the energy above which all flares are detected. λ_1 is the corresponding rate. α remains the power law exponent of the flare frequency distribution.

We are also given the posterior distribution for the rate λ_2 of flares above S_2 in Eq. (20) in Wheatland (2004):

$$\begin{aligned} P_2(\lambda_2) &= \int_1^\infty d\alpha \int_0^\infty d\lambda_1 \delta\left(\lambda_2 - \lambda_1 \cdot \left(\frac{S_1}{S_2} \right)^{\alpha-1}\right) \\ &\quad \cdot P_1(\lambda_1) \cdot P_\alpha(\alpha) \end{aligned} \quad (\text{G.2})$$

As we have additional information in the form of uncertainties in our data $S = \{S_i, \lambda_i, \sigma_{S,i}\}$, we can expand Eq. G.2 with this knowledge. Assuming that the observed flare energies S_i with cumulative rates λ_i are distributed around the real flare energies $S_{0,i}$ with Gaussian uncertainties $\sigma_{S,i}$, we can define:

$$\begin{aligned} p(S_i|\lambda_1, \alpha, \sigma_{S,i}) &= \frac{1}{2\pi\sqrt{\sigma_{S,i}}} e^{-\frac{(S_i - S_{0,i})^2}{2\sigma_{S,i}^2}} \\ &\quad - \frac{\left(S_i - S_1 \left(\frac{\lambda_i}{\lambda_1} \right)^{-1/(\alpha-1)} \right)^2}{2\sigma_{S,i}^2} \end{aligned} \quad (\text{G.3})$$

We assume in Eq. G.3 that uncertainties on λ_1 are negligible. Eq. G.2 then reads:

$$\begin{aligned} P_2(\lambda_2) &= \int_1^\infty d\alpha \int_0^\infty d\lambda_1 \delta\left(\lambda_2 - \lambda_1 \cdot \left(\frac{S_1}{S_2} \right)^{\alpha-1}\right) \\ &\quad \cdot P_1(\lambda_1) \cdot P_\alpha(\alpha) \cdot P_S(S|\lambda_1, \alpha, \sigma_S) \end{aligned} \quad (\text{G.4})$$

Table A.1. Membership catalogs overview. No distance are given for Hyades we adopted individual distances for all members.

source	type	clusters covered	notes
Curtis et al. (2013)	classifier	Rup 147	
Douglas et al. (2014)	probability	Hyades, Praesepe	meta study
Bouy et al. (2015)	probability	M35	DANCe
Gonzalez (2016)	classifier	M67	
Rebull et al. (2016a)	members list	Pleiades	meta study
Rebull et al. (2017)	classifier	Praesepe	meta study
Douglas et al. (2017)	members list	Praesepe	meta study
Gaia Collaboration et al. (2018a)	members list	Hyades, M35, Rup 147, Pleiades, Praesepe	Gaia DR2, (1)
Cantat-Gaudin et al. (2018)	probability	M35, Rup147, Pleiades, Praesepe	Gaia DR2
Gao (2018)	probability	M67	Gaia DR2
Reino et al. (2018)	probability	Hyades	Gaia DR1, (1)
Olivares et al. (2018)	probability	Pleiades	Gaia DR2, DANCe
Olivares et al. (2019)	probability	Rup 147	Gaia DR2, DANCe

Notes. DANCe: DANCe membership study project. (1) Positions for Hyades were propagated to epoch 2000 using Gaia proper motions.

with

$$P_S(S|\lambda_1, \alpha, \sigma_S) = C \prod_{i=1}^M p(S_i|\lambda_1, \alpha, \sigma_{S,i}). \quad (\text{G.5})$$

853 C absorbs the normalization, or evidence term.

854 Following Wheatland (2004), we marginalize over λ_1 using the
855 δ function in G.4 to obtain

$$\begin{aligned} P_2(\lambda_2) &= \int_1^\infty d\alpha \cdot P_1\left(\lambda_2 \cdot \left(\frac{S_2}{S_1}\right)^{\alpha-1}\right) \cdot P_\alpha(\alpha) \\ &\cdot P_S\left(S|\lambda_2 \cdot \left(\frac{S_2}{S_1}\right)^{\alpha-1}, \alpha, \sigma_S\right) \end{aligned} \quad (\text{G.6})$$

856 Transforming P_S into a function of ϵ with $\lambda_1 = -\ln(1-\epsilon)/\Delta T$
857 yields:

$$\begin{aligned} P_S(S|\epsilon, \alpha, \sigma_S) &= C \prod_{i=1}^M p(S_i|\epsilon, \alpha, \sigma_{S,i}) \\ &= \frac{C}{\Delta T(1-\epsilon)} \\ &\cdot \prod_{i=1}^M \left[\frac{1}{2\pi\sqrt{\sigma_{S,i}}} e^{-\frac{\left(S_i - S_2 \left(\frac{-\ln(1-\epsilon)}{\Delta T\lambda_i}\right)^{1/(\alpha-1)}\right)^2}{2\sigma_{S,i}^2}} \right] \end{aligned} \quad (\text{G.7})$$

858 Finally, P_S enters the joint posterior distribution from Eq. 2, that
859 becomes

$$\begin{aligned} p(\epsilon, \alpha) &= C \cdot (-\ln(1-\epsilon)^M) \\ &\cdot (\alpha-1)^M \cdot \Gamma(\alpha) \left[\frac{(S_2/S_1)^{M+1}}{\pi} \right]^\alpha \\ &\cdot (1-\epsilon)^{(T/\Delta T) \cdot (S_2/S_1)^{\alpha-1}-1} \\ &\cdot P_S(S|\epsilon, \alpha, \sigma_S). \end{aligned} \quad (\text{G.8})$$

Table B.1. Non-exhaustive literature overview over OC parameters.

cluster	source	distance [pc]	age [Myr]	[Fe/H]
M35	adopted in this work:	861	$147.5 \pm^{13.5}_{13.5}$	-0.21 ± 0.10
M35	Bossini et al. (2019) ^a		$402.7 \pm^{13.5}_{0.9}$	
M35	Cantat-Gaudin et al. (2018)	861		
M35	Netopil et al. (2016)			-0.21
M35	Scholz et al. (2015)	830	151	
M35	Geller et al. (2010)		133	
M35	Meibom et al. (2009)		$147.5 \pm^{13.5}_{13.5}$	
M35	Bragaglia and Tosi (2006)	912		
M35	Steinhauser and Deliyannis (2004)			-0.143 ± 0.014
M35	Barrado (2001)		180	
M35	Barrado et al. (2001)			-0.21 ± 0.10
M35	Sung and Bessel (1999)	832		
Rup 147	adopted in this work:	305	$2650 \pm^{380}_{380}$	0.08 ± 0.07
Rup 147	Bragaglia et al. (2018)			0.08 ± 0.07
Rup 147	Cantat-Gaudin et al. (2018)	305		
Rup 147	Gaia Collaboration (2018)	309	$1995 \pm^{404}_{257}$	
Rup 147	Torres et al. (2018)	283	$2650 \pm^{380}_{380}$	
Rup 147	Curtis (2016) ^b			0.10 ± 0.02
Rup 147	Scholz et al. (2015)	270	1953	
Rup 147	Curtis et al. (2013)	300	$3125 \pm^{125}_{125}$	0.07 ± 0.03
Pleiades	adopted in this work:	135.6	$135 \pm^{25}_{25}$	-0.037 ± 0.026
Pleiades	Bossini et al. (2019) ^a		$86.5 \pm^{2.4}_{2.4}$	
Pleiades	Cantat-Gaudin et al. (2018)	135.6		
Pleiades	Gossage et al. (2018)		$135 \pm^{25}_{25}$	
Pleiades	Yen et al. (2018)	126.3	$141.3 \pm^{170}_{100}$	
Pleiades	Chelli and Duvert (2016)	139		
Pleiades	Netopil et al. (2016)			-0.01
Pleiades	Dahm (2015)		$112 \pm^{5}_{5}$	
Pleiades	Scholz et al. (2015)	130	120	
Pleiades	Conrad et al. (2014)			-0.037 ± 0.026
Pleiades	Melis et al. (2014)	136		
Pleiades	Bell et al. (2012)	135	125	
Praesepe	adopted in this work:	185.5	$750 \pm^{3}_{3}$	0.16
Praesepe	Bossini et al. (2019)		$750 \pm^{3}_{7}$	
Praesepe	Cantat-Gaudin et al. (2018)	185.5		
Praesepe	Gossage et al. (2018)		590	
Praesepe	Yen et al. (2018)	183	$794 \pm^{253}_{269}$	
Praesepe	Netopil et al. (2016)			0.16
Praesepe	Scholz et al. (2015)	187	832	
Praesepe	Boesgaard et al. (2013)			0.12
Praesepe	Boudreault et al. (2012)	160	630	
Praesepe	Salaris et al. (2004)	175	650	
M67	adopted in this work:	908	$3639 \pm^{17}_{17}$	$-0.102 \pm .081$
M67	Bossini et al. (2019)		$3639 \pm^{17}_{17}$	
M67	Netopil et al. (2016)			0.03
M67	Scholz et al. (2015)		$3428 \pm^{147}_{72}$	
M67	Conrad et al. (2014)			$-0.102 \pm .081$
M67	Dias et al. (2012)	908	4300	
M67	Oñehag et al. (2011)	880	4200	0.02
Hyades	adopted in this work: ^c		$690 \pm^{160}_{100}$	0.13 ± 0.02
Hyades	Gaia Collaboration (2018)		$690 \pm^{160}_{100}$	
Hyades	Gossage et al. (2018)		680	
Hyades	Liu et al. (2016)			± 0.02
Hyades	Netopil et al. (2016)			0.13
Hyades	Taylor and Joner (2005)			0.103 ± 0.008
Hyades	Cummings et al. (2005)			0.146 ± 0.004
Hyades	Salaris et al. (2004)		650	0.15
Hyades	Perryman et al. (1998)		$625 \pm^{50}_{50}$	
Hyades	Martin et al. (1998)		$650 \pm^{70}_{70}$	

Article number, page 22 of 24
Notes. ^(a) Bossini et al. (2019) noted some caveats for their determination of ages of young clusters, for which they used Gaia DR2 photometry for isochrone fitting. ^(b) Curtis (2016) reanalysed HIRES spectra using an improved spectroscopic method as compared to Curtis et al. (2013). ^(c) We did not adopt a mean value for the Hyades distance because the cluster members are on average closer than 50 pc.

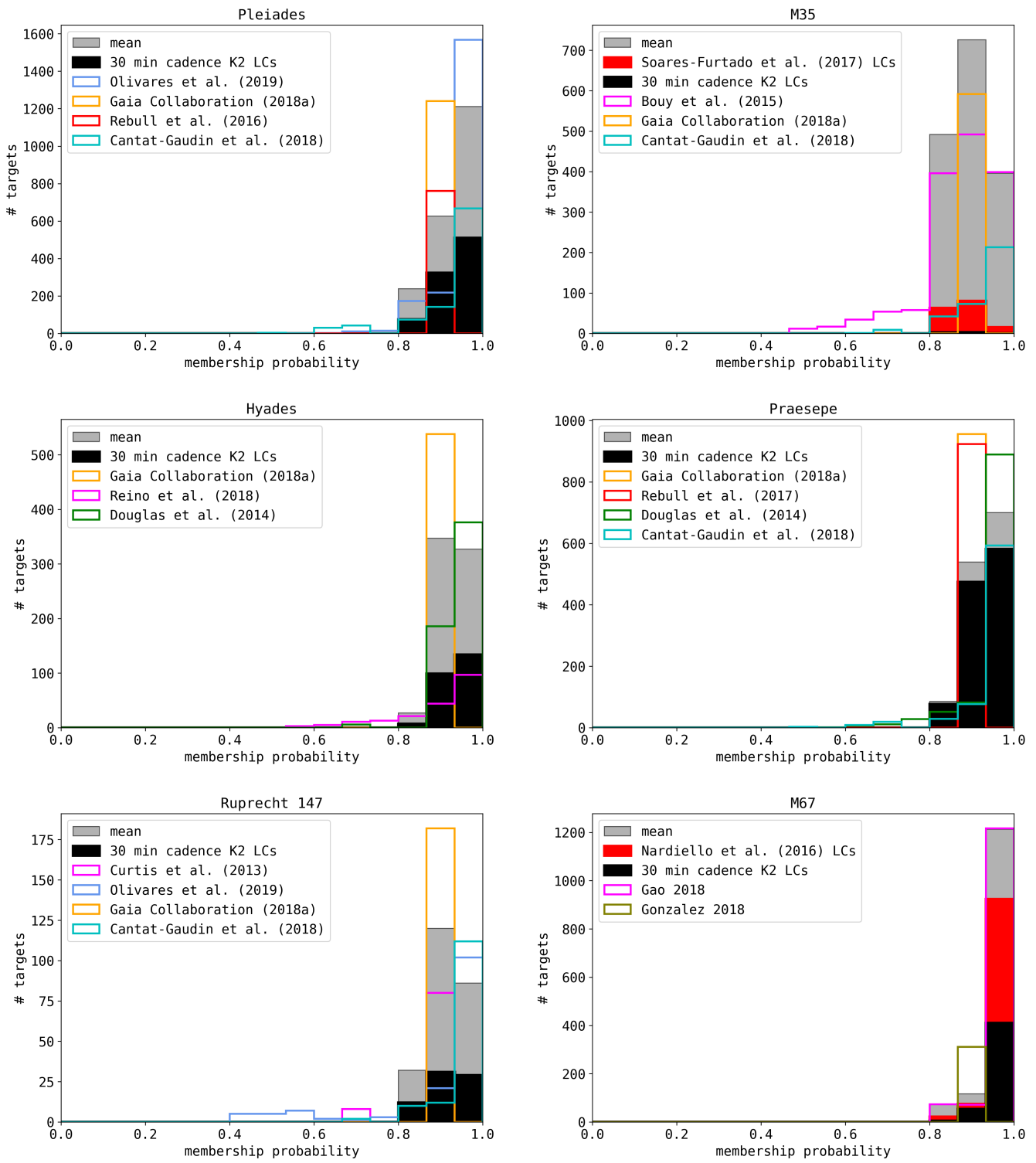


Fig. A.1. Membership histograms.

Table F.1. Literature overview over power law fitting approaches to FFDs.

Who	method	data	$\alpha - 1$
Hawley et al. (2014)	LSq with Poisson uncertainty, increase the low energy limit until the fit is robust		
Davenport (2016)	weighted LSq, asymmetric Poisson confidence intervals following Gehrels1986		
Gizis (2017)	de-biased MLE (Arnold2015), weight each point with $\text{sqrt}(N)$ in each bin (Clauset+2009)		
Paudel et al. (2018)	ML from a paper in 2010, used emcee (Foreman-Mackey2013)		
Lacy (1976)	graphical, linear LSq	386 flares on UV Cetis	.43-1.
Güdel et al.(2003)	-		
Davenport et al. (2012)	Fit $\log_{10} Y = \alpha + (\beta \log_{10} X)(10 - \gamma/(X + \delta))$	~50,000 M dwarfs from SDSS and 1321 M dwarfs from 2MASS	.9-2.1
Lurie et al. (2015)	Bayesian Markov chain Monte Carlo based algorithm (Kelly 2007) for linear regression	2 dMe5 dwarfs	.92-1.03
Audard et al. (2000)	Crawford+1970 MLE (Jauncey-style)	EUVE 12 F-M type stars, 10-20 flares each	.46-1.61
Shakhovskaia (1989)	linear representation, power laws from Gershberg/Shakhovskaya1983	30-40 dK0-dM8, 200 flares	.4-1.4
Yang et al. (2017)	binned FFDs	103187 flares on 540 M-type dwarfs in Kepler	1.07 +/- 0.35
Howard et al. (2018)			